ACS Catalysis

Research Article

Cite This: ACS Catal. 2020, 10, 494−509

pubs.acs.org/acscatalysis

Mechanistic Insights into pH-Controlled Nitrite Reduction to Ammonia and Hydrazine over Rhodium

Chelsea A. Clark,[†,¶,▽] C. Prakash Reddy,[‡,▽] Hao Xu,[§,▽] Kimberly N. Heck,[†,¶] Guohua Luo,[§] Thomas P. Senftle,*[,†,‡] and Michael S. Wong*[,†,∥,⊥,#,¶]

[†]Department of Chemical and Biomolecular Engineering, [∥]Department of Chemistry, and [⊥]Department of Civil and Environmental Engineering, Rice University, 6100 Main Street, Houston, Texas 77005-1892, United States

[‡]Applied Physics Program, [#]Department of Materials Science and NanoEngineering, and [¶]Nanosystems Engineering Research Center for Nanotechnology-Enabled Water Treatment, Rice University, 6100 Main Street, Houston, Texas 77005, United States

[§]Beijing Key Laboratory of Green Chemical Reaction Engineering and Technology, Department of Chemical Engineering, Tsinghua University, Beijing 100084, China

Supporting Information

ABSTRACT: An unintended consequence of industrial nitrogen fixation through the Haber−Bosch process is nitrate (NO_3^-) and nitrite (NO_2^-) contamination of ocean, ground, and surface waters from fertilizer runoff. Transition-metal catalysts, particularly those based on Pd, are effective in removing NO_3^-/NO_2^- through reduction to N_2 or NH_4^+. Pd is regarded as the most effective metal for NO_3^-/NO_2^- reduction, and as such, few studies have thoroughly explored the performance of other transition metals as a function of varying reaction conditions. In this work, we investigated the NO_2^- reduction properties of alumina-supported Rh using Pd as a benchmark, where we varied the bulk solution pH to probe the effect of reaction conditions on the catalytic chemistry. Pd expectedly showed a high reduction activity (289 L/g-surface-metal/min) and a high N_2 selectivity (>99% at 20% conversion) at low pH and near inactivity at high pH. Surprisingly, the Rh catalyst, while inactive at low pH, showed moderate activity (22 L/g-surface-metal/min) and high NH_4^+ selectivity (>90% at 20% conversion) at high pH. Hydrazine (N_2H_4) was also detected as a reaction intermediate when NH_4^+ was formed. Microkinetic models built with energetics from density functional theory reveal that Rh catalysts are poisoned by NO* at low pH because of the rapid dissociative adsorption of protonated nitrite (HNO_2) under acidic conditions, which was confirmed by in aqua surface-enhanced Raman spectroscopy. NO* poisoning of the Rh surface lessens at increased solution pH because NO_2^- does not dissociate as readily compared to HNO_2, which explains why Rh exhibits higher activity in basic solutions. The microkinetic models further elucidate the competition between N_2H_4 and NH_3/NH_4^+ formation as a function of pH, where we find that hydrogen surface coverage dictates product selectivity. These results update the common view that only Pd-based catalysts are effective for NO_2^- reduction and suggest unexplored avenues for nitrogen chemistry.

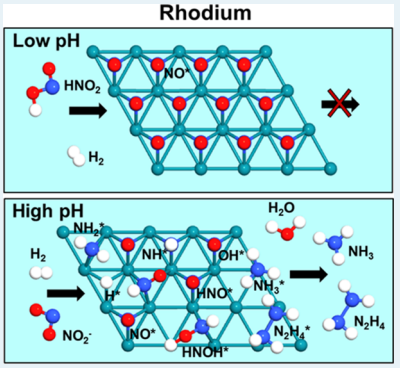

KEYWORDS: *catalytic denitrification, rhodium catalyst, hydrazine detection, density functional theory, micro-kinetic model, surface-enhanced Raman spectroscopy*

1. INTRODUCTION

Nitrogen fixation is a fundamentally important chemical process for the survival of all living organisms because of the fact that atmospheric dinitrogen (N_2) is not bioavailable for plants and animals to utilize. The Haber−Bosch (H−B) process, which is an industrial process that reduces atmospheric N_2 to ammonia (NH_3), revolutionized the agricultural industry, with approximately 80% of manufactured NH_3 being used for the production of agricultural fertilizers.[1,2] The synthetic fertilizer produced from H−B and similar processes is estimated to be responsible for feeding almost 50% of the world's population.[3,4] Unfortunately, the efficiency of nitrogenous fertilizer use is remarkably low, leading to the pollution of ocean, ground, and surface waters with nitrate (NO_3^-) and nitrite (NO_2^-) runoff. It is estimated that ∼20% of the nitrogen applied as fertilizer globally is lost because of leaching, with the primary loss pathways being the conversion of NH_3 to NO_3^- and NO_2^- by nitrifying bacteria in the soil and the conversion of NO_3^- back to N_2 by denitrifying bacteria.[4−6] Nitrate/nitrite anions have significant adverse health effects in humans, which include diseases such as methemoglobinemia (blue baby syndrome) as well as cancer and hypertension caused by metabolic conversion of nitrite into *N*-nitroso compounds.[7−10]

Received: July 31, 2019
Revised: November 22, 2019
Published: November 27, 2019

DOI: 10.1021/acscatal.9b03239
ACS Catal. 2020, 10, 494−509

Over the past two decades, catalytic reduction of environmental water contaminants has garnered attention as a promising technology because of its potential for high degradation activity and relatively low energy intensity.[11,12] These catalysts can directly degrade nitrate/nitrite anions under reductive conditions, potentially offering a more efficient method for denitrification compared with more traditional methods, such as ion exchange or reverse osmosis. Since the first reports on the chemistry of nitrate/nitrite hydrogenation by Vorlop and Tacke, Pd-based catalysts have been the most widely investigated materials for this reaction.[13−15] Monometallic Pd itself shows very low activity for the reduction of nitrate and requires a secondary promoter metal (usually Cu, In, or Sn) to catalyze the initial reduction of nitrate to nitrite.[16−19] Pd-based catalysts demonstrate both high nitrite reduction activity under ambient conditions and high selectivity to harmless N_2 over contaminating NH_3/NH_4^+.[14,15,17,20−22]

Other noble metals (such as Pt, Rh, Ru, and Ir) are regarded as being less active for nitrite reduction and less selective to dinitrogen, compared to Pd.[14,15] However, these conclusions may not be entirely valid as they are based on reaction conditions that favor Pd reduction catalysis. Hörold et al. first identified reaction pH as a governing factor in nitrate/nitrite hydrogenation, affecting both the nitrite conversion rate and ammonium selectivity.[15] Low pH values favor the conversion of nitrite to dinitrogen. Hydroxyl anions are generated during the course of the reaction, and therefore, an increase in pH leads to decreased activity, unless the reaction is buffered (Scheme 1). There are very few studies on pH effects on nitrate/nitrite hydrogenation for other metals, with the exceptions of Pt and Ru.[23−25] The pH effect is well-observed but poorly understood.

Scheme 1. Two Reactions of Nitrite Reduction, Leading to Dinitrogen and Ammonia (with Free Energy Values at 25 °C, 1 M Reactant Concentrations, 1 atm)

$$2NO_2^- + 3H_2 \rightarrow N_2 + 2H_2O + 2OH^- \quad \Delta G^\ominus = -428 \text{ kJ mol}^{-1}$$

$$NO_2^- + 3H_2 \rightarrow NH_3 + H_2O + OH^- \quad \Delta G^\ominus = -508 \text{ kJ mol}^{-1}$$

Rh is an intriguing metal to study for nitrate/nitrite hydrogenation catalysis. Rh-based catalysts are effective for related reactions, such as gas-phase NO_x reduction, liquid-phase reduction of nitroaromatic compounds, and electrocatalytic reduction of nitrate.[26−31] The early work of Hörold et al. showed that the Rh metal loading normalized activity was approximately one-third of that of Pd at pH 6,[14,15] but few studies followed. It remains unclear whether Pd remains more active than Rh under alternative reaction conditions, particularly outside of pH ≈ 5−6.[32] The literature is inconsistent with regard to the selectivity to N_2 versus NH_4^+ over Rh catalysts.[15,20,32]

In this work, we sought to establish a mechanistic understanding of the pH effect on nitrite hydrogenation over an alumina-supported Rh catalyst using the well-established behavior of alumina-supported Pd for comparison. We carried out batch-reactor studies in a wide pH range (i.e., pH 4 to pH 11.5) and estimated pseudo-first-order rate constants for the nitrite reaction while measuring the concentrations of detected reaction products. These studies show an opposite trend in NO_2^- reduction over Pd and Rh, where Rh primarily forms NH_3 and is only active at high pH and, expectedly, Pd rapidly forms N_2 at low pH. Density functional theory (DFT) calculations were performed to understand the pH-dependent activity and selectivity of Rh. We found that there is a strong thermodynamic driving force and a low kinetic barrier for protonated nitrite (HNO_2) to dissociatively adsorb on Rh as NO* and OH*. The kinetics of NO* dissociation and hydrogenation are slow, which leads to NO* surface poisoning at low pH. At higher pH, the nitrite in solution is predominantly a deprotonated anion (NO_2^-), which we found has a higher adsorption and dissociation barrier. Thus, surface NO* poisoning is relieved at higher pH. These predictions were corroborated by in aqua surface-enhanced Raman spectroscopy (SERS), which confirmed that high NO* surface coverage is observed only under low pH conditions. We also evaluated competitive N_2H_4 versus NH_3/NH_4^+ formation rates, which is correlated with surface hydrogen coverage, reflecting the balance between hydrogenation and coupling of nitrogen-containing surface intermediates.

2. EXPERIMENTAL SECTION

2.1. Materials. Commercial Rh/Al_2O_3 and Pd/Al_2O_3 catalysts (metal content of 1 wt %) were purchased from Alfa Aesar, which were reported to be in the reduced form. Sodium nitrite ($NaNO_2$ > 99.5%) and monobasic sodium phosphate (NaH_2PO_4 > 99.5%) were purchased from Fisher. Dibasic sodium phosphate (Na_2HPO_4 > 99%), ammonium chloride (NH_4Cl ≥ 99.5%), sulfanilamide (≥99%), *N*-(1-naphthyl)ethylenediamine (>98%), 4-dimethylaminobenzaldehyde (>99%), concentrated phosphoric acid (H_3PO_4, >85%), concentrated sulfuric acid (H_2SO_4, 95−98%), and hydrazine (35 wt % N_2H_4 in H_2O) were all purchased from Sigma-Aldrich. Nessler's reagent was purchased from Macron. Hydrogen gas (99.999%) was purchased from Matheson. All experiments were conducted using deionized (DI) water (>18 MΩ·cm, EMD Millipore Synergy).

2.2. Catalyst Characterization. *2.2.1. Transmission electron microscopy.* Transmission electron microscopy (TEM) was performed on a JEOL JSM 2010 microscope (operation voltage of 200 kV). TEM samples were prepared by suspending ∼10 mg of catalyst in 10 mL of ethanol and ultrasonicating for 30 min to disperse the sample. Four drops of this solution were placed onto a carbon-coated copper grid and then dried in a desiccator for 12 h at room temperature to ensure complete ethanol evaporation.

2.2.2. X-ray diffraction. X-ray diffraction (XRD) measurements were performed on a Rigaku D/Max Ultima II diffractometer using Cu Kα (λ_{avg} = 1.5418 Å) radiation. Samples were measured with the detector tube set to 40 kV and 40 mA, 1° divergence and scattering slits, a 0.30 mm receiving slit, and a 10.00 mm divergence height-limiting slit width. The scan speed was 1.5°/min with a sampling width of 0.02°.

2.2.3. CO Pulse Chemisorption. CO pulse chemisorption was performed using a Micromeritics AutoChem II 2920 analyzer. The catalysts were heated to 350 °C (10 °C/min ramp rate) under flowing 10% H_2/Ar and soaked at 350 °C for 1 h to ensure full reduction of the metal and then for another 1.5 h under flowing He. The samples were cooled to 35 °C before a known volume of CO was injected under a constant He flow, until no more CO was adsorbed (as detected by the thermal conductivity detector). All gas flow rates were set to 50 cm^3/min at standard temperature and pressure. The metal dispersion and particle size values were estimated assuming a

DOI: 10.1021/acscatal.9b03239
ACS Catal. 2020, 10, 494−509

1:1 CO/metal-atom stoichiometry and a hemispherical particle shape.[33−35]

2.2.4. N_2 Adsorption Analysis. The Brunauer−Emmett−Teller (BET) specific surface areas were calculated from N_2 adsorption isotherms obtained at liquid-N_2 temperature (77 K) using an Autosorb-iQ-MP system. Before measurements, the sample was degassed for 12 h under vacuum (~2 mmHg) at 200 °C. The average pore size was calculated using nonlocal DFT assuming a cylindrical pore shape.

2.2.5. SERS Analysis. Palladium-covered and rhodium-covered gold nanoshells ("Au@Pd NSs" and "Au@Rh NSs") supported on silicon wafers were prepared in the same manner as reported previously[36−38] but with a higher Pd (or Rh) metal loading [~100% calculated Pd (or Rh) surface coverage of the Au NS surface]. Briefly, the Au NSs were prepared by adding 400 μL of aminated silica colloid (120 nm diameter, Nanocomposix) to 20 mL of 2-week-old Au NPs prepared by the Duff method and aged overnight.[39] This mixture was then centrifuged and redispersed twice to remove free Au NPs and concentrated into ~3 mL volume. The Au-decorated silica colloid suspension (30 μL) was then added to 3 mL of 370 μM $HAuCl_4$ and 18 mM K_2CO_3 solution and stirred. Formaldehyde (30 μL, 30 wt %) was used to reduce the gold salt onto the cores, creating a continuous shell. Comparing the ultraviolet-visible (UV−vis) spectra to that predicted by the Mie theory indicated a shell thickness of ~22 nm with a concentration of 1.18×10^8 particles/mL. To a 3 mL sol of as-synthesized Au NS, 6 μL volume of a stock solution of H_2PdCl_4 or $Rh(NO_3)_3$ (2.49 mM) was added. The metals were reduced onto the Au NS surface by bubbling with H_2 gas (100 sccm) for 1.5 min. Damping of the NS plasmon was observed via UV−vis spectroscopy (Shimadzu UV-2401, slit width = 0.2 cm) giving indirect evidence of metal reduction onto the Au (the dielectric functions of Rh[40] and Pd[41] have large ϵ_2 at visible light frequencies). Following the reduction step, the NSs were centrifuged and the supernatant was removed, leaving behind a fluid volume of 300 μL. The concentrated shells of 20 μL volume (concentration = 1.18×10^9 NS/mL) were added to the poly(vinylpyrolidone)-coated silicon chips. The next day, the chips were rinsed with DI water before affixing to a microscope coverslip and plasma cleaned prior to introduction into the SERS reaction chamber, as previously reported.

Chemisorption SERS experiments were performed analogously to our previous works.[36,37] Nitrite solutions (5 ppm-NO_2^-) were prepared at two different pH values and buffered with 25 mM phosphate buffer at 3.1 for the "low-pH" solution and 9.4 for the "high-pH" solution. The solutions were bubbled with nitrogen gas for 15 min to displace the dissolved O_2 and fill the headspace. Nitrite-free solutions at high and low pH were also prepared and bubbled with N_2 or H_2 gas for baseline measurements and catalytic metal regeneration. After introduction of inert or reaction solution, measurements were taken using a Renishaw Raman microscope with a 785 nm laser using 0.5% laser power in the range of 100−2200 cm^{-1}. Each measurement took approximately 60 s. To correct for possible drift of the focal plane, the Raman spectra were normalized to the silicon peak at 520 cm^{-1}.

2.3. Catalytic Experiments. Prior to the experiments, the as-purchased Rh/Al_2O_3 catalyst was treated under flowing H_2 (100 sccm) at ~200 °C for 1 h before use. This was done to maintain reproducibility of the results. For our convenience, the as-purchased Pd/Al_2O_3 catalyst was not treated before use, after we confirmed that the reductive treatment step had no effect on the observed activity (which is due to the ease of Pd reducibility during reaction testing). Batch nitrite reduction experiments were conducted in 125 mL glass bottles with poly(tetrafluoroethylene) (PTFE)-lined threads and PTFE−silicone septum caps. The initial solution volume was fixed at 50 mL. Six initial pH values ranging from 4 to 11.5 (with a pH step size of 1.5) were selected. pH values lower than 4 were not considered because Rh catalyst activity was negligible. pH values higher than 11.5 also were not considered because of dissolution of the alumina support (see Table S1). To prevent the pH of the reaction medium from changing significantly during the reaction, monobasic sodium phosphate and/or dibasic sodium phosphate (final concentration of 25 mM) were added as a buffer, with further pH adjustments made with either H_3PO_4 or NaOH. The ionic strength values at pH 4, 5.5, 7, 8.5, 10, and 11.5 were 25, 29, 50, 71, 75, and 78 mM, respectively. Without the buffer, the pH increased from 6.5 to >10 at the end of nitrite reduction testing (Figure S1). Final pH values for the buffered reactions are given in Table S2.

The experimental conditions of 25 mg catalyst charge and 600 rpm stir rate were optimized to ensure that the reaction was kinetically limited and not mass-transfer limited. This analysis is detailed in the Supporting Information (Figure S2). Before each experiment, the reactor (containing the buffer solution and catalyst powder) was purged with H_2 for 15 min at a flow rate of 100 mL/min to remove the dissolved oxygen and fill the headspace. All experiments were carried out in triplicate at room temperature (~23 °C) and atmospheric pressure. The reactions were initiated by injecting 250 μL of concentrated $NaNO_2$ solution (10 mg-NO_2^-/mL) into the batch reactor for a starting NO_2^- concentration of 50 ppm-NO_2^- (~1 mM). Samples were collected at 0, 3.75, 7.5, 15, 30, 45, 60, 120, 240, and 360 min, as needed, and passed through a 0.2 μm filter to separate the catalyst from the reaction medium.

Three species were detected (NO_2^-, NH_4^+, and N_2H_4) and their concentrations were determined colorimetrically using UV−vis spectroscopy (Shimadzu UV-2401, slit width = 0.2 cm). Griess's reagent was used to quantify the concentration of NO_2^- (limit of detection of 0.2 ppm-NO_2^-). Nessler's reagent was used to quantify the concentration of NH_4^+ (limit of detection of 0.1 ppm-NH_4^+). Ehrlich's reagent was used to quantify the concentration of N_2H_4 (limit of detection of 0.05 ppm-N_2H_4).

Because H_2 gas was in excess, the observed reaction rate constant k was calculated assuming a pseudo-first-order dependence on the nitrite concentration within the first 2 h of reaction

$$-\frac{dC_{NO_2^-}}{dt} = kC_{NO_2^-} \quad (1)$$

where $C_{NO_2^-}$ is the nitrite concentration in mg/L and t is the reaction time in minutes.

The initial surface metal-normalized rate constant k_{cat} (in L $g_{surface\ metal}^{-1}$ min^{-1}) was then calculated from k (via $k_{cat} = k/C_{cat}$), where C_{cat} (in $g_{surface\ metal}^{-1}$ L^{-1}) is calculated according to the metal loading and percent dispersion obtained from CO chemisorption.

The selectivity values to ammonium ($S_{NH_4^+}$) and hydrazine ($S_{N_2H_4}$) were calculated from the following equations

DOI: 10.1021/acscatal.9b03239
ACS Catal. 2020, 10, 494−509

$$S_{NH_4^+} = \left(\frac{C_{NH_4^+}}{C_0 - C}\right) \times 100\% \quad (2)$$

$$S_{N_2H_4} = \left(\frac{2 \times C_{N_2H_4}}{C_0 - C}\right) \times 100\% \quad (3)$$

where C_0 and C are the initial molar concentrations of nitrite and the concentration of nitrite at time t, respectively. Nitric oxide (NO) was assumed to be absent as a reaction byproduct, based on previous isotopic labeling studies.[19] Minor amounts of N_2O have occasionally been detected in the bulk as a transient intermediate during nitrite reduction with 100% selectivity to N_2.[19,24] In this work, their concentrations were not quantified, and it was estimated that N_2 accounted for the rest of the nitrogen balance during nitrite reduction.

2.4. Computational Methodology. DFT calculations were performed using the Vienna Ab initio Simulation Package (VASP 5.4.4).[42] The exchange−correlation functional was treated with the Perdew−Burke−Ernzerhof[43] generalized gradient approximation within the projector-augmented-wave formalism.[44,45] The $4d^85s^1$, $4d^{10}$, $2s^22p^4$, $2s^22p^3$, and $1s^1$ valence electrons were treated self-consistently for Rh, Pd, O, N, and H, respectively. All calculations were spin-polarized, and the kinetic energy cutoff for plane wave basis sets was 450 eV. The Methfessel−Paxton smearing method[46] was employed with a smearing width of 0.2 eV. The Brillouin zone was sampled using a 7 × 7 × 7 Monkhorst−Pack[47] (MP) k-point grid for bulk Rh and Pd unit cells, and a 4 × 4 × 1 MP grid was used for the 3 × 3 × 1 simulation cell of Rh(111) and Pd(111) surface facets. van der Waals corrections were included by employing the Grimme's D2 dispersion correction.[48]

The atomic force convergence cutoff for all geometry optimizations was 0.02 eV $Å^{-1}$, where convergence to an energy minimum was verified in each case with a frequency calculation to ensure that all imaginary frequencies were eliminated. Frequency calculations were completed with finite differences of ±0.02 Å with only atoms in the adsorbed species populating the Hessian (i.e., all metal atoms in the surface were fixed). The climbing image nudge elastic band (NEB)[49,50] method was employed to identify the transition states. Frequency calculations confirmed that each transition state structure has only one imaginary frequency corresponding to the saddle point of the reaction coordinate. All optimized structures, total DFT energies, and vibrational frequencies are reported in the Supporting Information.

Optimization of the bulk lattices of Pd and Rh resulted in lattice constants of 3.89 and 3.77 Å, respectively, which are in good agreement with the respective experimental values of 3.89 and 3.80 Å.[51] We chose the (111) facet of Pd and Rh as our surface models in this study because these surfaces are the most stable,[52] and all reported DFT results are computed with the Rh(111) or Pd(111) surface models. However, since these surfaces are the most stable, they are also expected to yield high activation barriers for elementary reactions occurring on the surface. Thus, we take our predicted barriers to represent the ceiling for the actual barriers, yielding lower rates than what is experimentally measured over metallic clusters that expose more reactive undercoordinated reaction sites. As the nature of these sites is unknown, we prefer to use the (111) facet model as a conservative choice for studying activity trends with respect to solution pH. We introduce a barrier scaling parameter in our kinetic models to test the sensitivity of our analysis against the possibility of lower reaction barriers. This sensitivity analysis is presented in the Supporting Information in Figure S3, where we find that, although overall rates are sensitive to barrier heights, the activity trends with respect to solution pH are not. Catalyst surfaces were modeled using slab geometries with four layers that each contain nine metal atoms. The bottom layer of the slab was fixed to approximate the underlying bulk, and a vacuum layer of at least 15 Å was used to separate periodic slabs in the z-direction. Isolated molecules were treated with a 15 × 15 × 15 Å simulation cell and a 1 × 1 × 1 MP grid.

Free energies for all structures were computed using standard formulae[53] derived from statistical mechanics to account for translational, rotational, vibrational, and electronic degrees of freedom. Translational and rotational contributions to the free energy were excluded for all surface-adsorbed species. Multiple models were tested to account for the entropy of transition states involving the adsorption or desorption of molecular species at the surface, in which the molecule can retain varying amounts of translational entropy in the transition state (i.e., ranging from a fully adsorbed state with no translational degrees of freedom to a preadsorbed state with two-dimensional translational freedom).[54] We found that varying the translational entropy between these two extremes did not alter our conclusions, as demonstrated by a sensitivity analysis reported in the Supporting Information in Figure S4. Reaction free energies were calculated at a temperature of 300 K, a H_2 pressure of 1 atm, a nitrite concentration of 50 ppm, a NH_3 concentration of 2.5 ppm, a N_2H_4 concentration of 1 ppm, and a H_2O concentration of 55 M. For each adsorbate, the energy of the most favorable adsorption site is reported, where adsorption on all high-symmetry fcc, hcp, bridge, and top sites for each adsorbate was tested.

The free energy of charged species in solution was computed as a function of solution pH using thermodynamic cycles and experimental acid dissociation constants with the following relationships

$$G_{NH_4^+} = G_{NH_3} + \Delta G_{protonation} \quad (4)$$

$$G_{NO_2^-} = G_{HNO_2} + \Delta G_{deprotonation} \quad (5)$$

$$\Delta G_{protonation} = 2.303 \cdot RT \cdot (pH - pK_a) \text{ and}$$
$$\Delta G_{deprotonation} = -\Delta G_{protonation} \quad (6)$$

where G_{NH_3} and G_{HNO_2} are the Gibbs free energies of neutral molecules computed with DFT and statistical mechanics, and $\Delta G_{protonation}$ and $\Delta G_{deprotonation}$ are the protonation and deprotonation energies, respectively, of the neutral molecule computed with the experimental pK_a of the molecule and the pH of the solution. We employ pK_a values of 3.25 and 9.25 for HNO_2 and NH_3, respectively.[55] We considered two reaction paths for the dissociative adsorption of nitrite to account for the effect of pH on the preferred reaction mechanism, that is, we expect that dissociation of HNO_2 will be most relevant under acidic conditions when the protonated form of nitrite dominates, whereas the adsorption of NO_2^- will be relevant under basic conditions. The apparent activation barrier for the dissociative adsorption of HNO_2 was computed with the following sequence of elementary reactions

$$NO_2^- + H^+ \rightleftharpoons HNO_2 \quad (7)$$

DOI: 10.1021/acscatal.9b03239
ACS Catal. 2020, 10, 494−509

Scheme 2. Proposed Reaction Pathways for the Reduction of NO_2^- Leading to the Formation of NH_3/NH_4^+ (Blue), N_2H_4 (Red), and N_2 (Orange); Green Labels Correspond to Elementary Reactions Except for R22, Which Lumps Multiple Elementary Steps That Are Not Shown

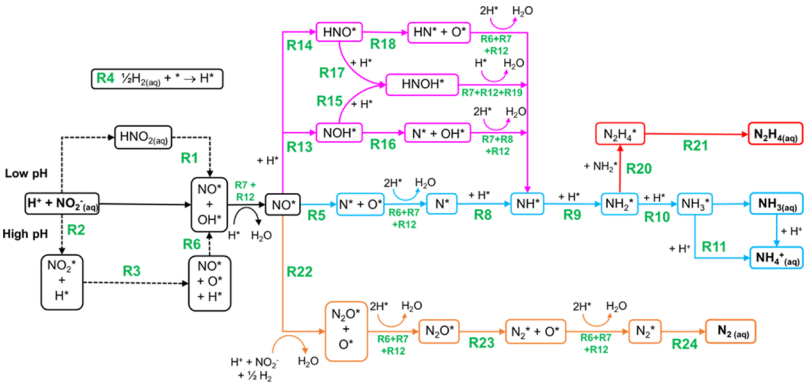

$$HNO_2 + 2^* \rightarrow NO^* + OH^* \quad (8)$$

The apparent dissociation barrier for the overall reaction ($NO_2^- + H^+ + 2^* \rightarrow NO^* + OH^*$) is computed as the sum of the protonation energy required to form HNO_2 in solution (which is pH-dependent) and the reaction barrier required to dissociate HNO_2 over the catalyst surface. We do not consider the nondissociative adsorption of HNO_2 as we found that HNO_2 dissociation is highly exergonic and is effectively barrierless over both Rh and Pd (see Figure S5 for NEB calculations). The apparent barrier for this process will become prohibitively large under very basic conditions. Therefore, we also consider the direct adsorption and dissociation of NO_2^- with the following sequence of elementary reactions

$$NO_2^- + H^+ + 2^* \rightarrow NO_2^* + H^* \quad (9)$$

$$NO_2^* + * \rightarrow NO^* + O^* \quad (10)$$

$$O^* + H^* \rightarrow OH^* + * \quad (11)$$

The direct adsorption of NO_2^- on the surface and its conversion to NO_2^* involves transfer of negative charge from NO_2^- to the surface, where it is assumed that this charge is quenched by coupled proton adsorption to form H*. Both the nitrite adsorption processes, either through direct NO_2^- adsorption or through HNO_2, are included in the microkinetic model, where the preferred reaction path is determined by the pH of the solution and the apparent barrier of each process. HNO_2 dissociation to NOH* and O* was also considered, and we found a barrier of 0.77 eV for this reaction over the Rh surface. This high barrier suggests that HNO_2 dissociation to NOH* and O* will not compete with the NO* and OH* formation path that has no activation barrier.

Solvation was treated implicitly using the VASPsol[56,57] continuum implementation with a dielectric constant of 78.4 for water. Solvation energy was included as a single-point correction to geometries relaxed in vacuum. We also tested mixed explicit–implicit solvation models for molecular species and found that explicitly solvating the lone pairs of both ammonia and hydrazine with hydrogen bonds to water molecules leads to significantly enhanced stabilization of the molecule in solution. Thus, we apply the mixed explicit–implicit solvation correction to $NH_{3(aq)}$ and $N_2H_{4(aq)}$ in our main analysis. For comparison, we also report in the Supporting Information results derived with the implicit-only solvation model. The inclusion of the explicit water changes the overall rate of NH_3 and N_2H_4 production but does not alter the relative activity/selectivity trends with respect to pH (Figure S6).

We used the DFT energetics to build a microkinetic model for analyzing nitrite reduction to NH_3 and N_2H_4 at varying solution pH over Rh. Twenty-one elementary reactions, summarized in Table S4 and S5, were included in the microkinetic model. The rate constant of each elementary reaction was calculated using the Eyring–Polanyi–Evans equation

$$k = \frac{K_B T}{h} e^{-\Delta G^\dagger / RT} \quad (12)$$

$$k = \frac{K_B T}{h} e^{\Delta S^\dagger / R} e^{-E_a^\dagger / RT} \quad (13)$$

where k is the rate constant of the reaction step, K_B is the Boltzmann constant, T is the temperature, h is the Planck's constant, R is the gas constant, $\Delta G^\dagger$ is the Gibbs free energy of activation, $\Delta S^\dagger$ is the entropy of activation, and $E_a^\dagger$ is the activation energy. The employed values for the change in entropy ($\Delta S^\dagger$) and activation energy ($E_a^\dagger$) are listed in Table S4, and the values for change in free energy ($\Delta G^\dagger$) are listed in Table S5. Rate expressions (including forward and backward reactions) are obtained using the following equation

$$r_n = k_n \prod_i \theta_i^{\eta_{i,n}} \quad (14)$$

where r_n is the rate of the reaction n, k_n is the calculated rate constant, θ_i is the concentration of chemical species i in the reaction step n, and $\eta_{i,n}$ is the stoichiometric coefficient of species i in the reaction step n. Using the net rate expression of each species, the rate of coverage change is calculated using the equation

$$\frac{d\theta_i}{dt} = \sum_n \eta_{i,n} r_n \quad (15)$$

Equation 15 is a set of coupled differential equations, which is combined with a site balance and integrated numerically to obtain the coverage of each species as a function of time. A degree of rate control, $\bar{X}_{RC}$,[58,59] analysis was performed to identify rate-controlling elementary reaction steps during NO_2^- reduction to NH_3 and N_2H_4. Further details regarding $\bar{X}_{RC}$ are provided in the Supporting Information.

DOI: 10.1021/acscatal.9b03239
ACS Catal. 2020, 10, 494–509

Table 1. Structural Characteristics of Pd/Al_2O_3 and Rh/Al_2O_3 (1 wt % Metal Loading)

catalyst	metal dispersion from CO chemisorption (%)	particle size from CO chemisorption (nm)	TEM particle size (nm)	BET surface area (m^2/g)	average pore diameter (nm)
Pd/Al_2O_3	28	3.4	3.3 ± 0.5	147	12
Rh/Al_2O_3	65	1.7	1.9 ± 0.5	150	11

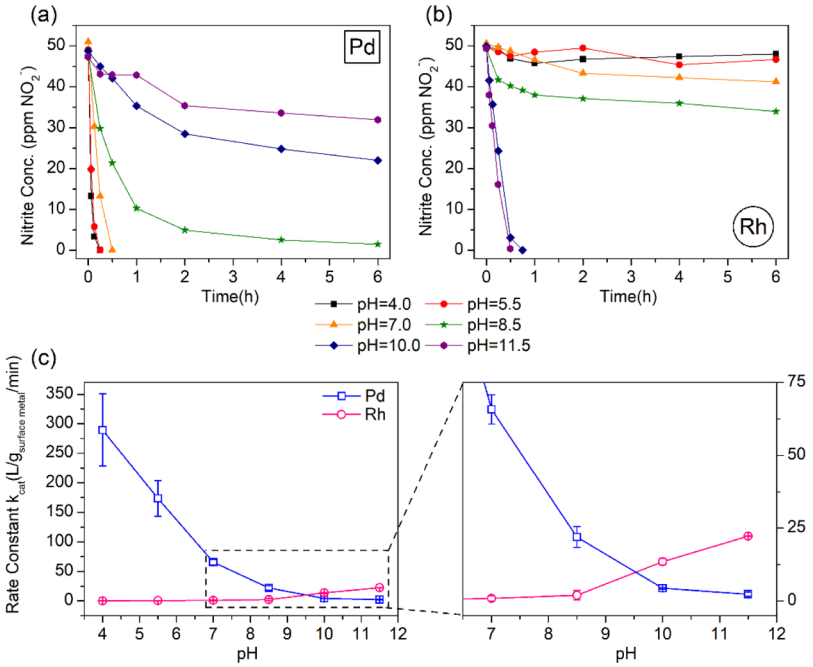

Figure 1. (a,b) Nitrite concentration vs time during the nitrite reduction reaction with 1 wt % Pd/Al_2O_3 and Rh/Al_2O_3 with 25 mM phosphate buffer at different initial pH values. (c) Initial first-order rate constant of nitrite reduction with 1 wt % Pd/Al_2O_3 and Rh/Al_2O_3 at different initial pH values. The right panel shows the data points in the pH 7−11.5 range.

3. RESULTS AND DISCUSSION

3.1. Nitrite Reduction Pathways. The reaction network for nitrite reduction is complex, with many possible reaction paths that branch to yield N_2, NH_3, or N_2H_4.[23,24,60] The reaction network investigated in this study is summarized in Scheme 2. The reaction begins with the adsorption of nitrite, which can either begin with NO_2^- adsorption followed by dissociation or with the direct dissociative adsorption of HNO_2 to form NO* and OH* (* indicates that the species is adsorbed). This will depend on the protonation state of the nitrite anion, which in turn is determined by the pH of the solution. Following NO_2^- adsorption and dissociation, OH* is removed from the surface through reaction with H* to form H_2O, where H* is generated from the dissociative adsorption of H_2. Over precious metal catalysts, adsorbed NO* is a crucial intermediate that dictates reaction selectivity.[19,23,61] NO* can either dissociate directly to form N* and O* (i.e., the blue-colored path in Scheme 2)[62] or can undergo hydrogenation to form HNO*, NOH*, and HNOH* prior to the dissociation of the N−O bond (i.e., the pink-colored paths in Scheme 2). NH* is hydrogenated to form NH_2^*, which can undergo further hydrogenation to form NH_3^*/NH_4^+ or can couple to form N_2H_4.

N_2H_4 was observed experimentally (see Section 3.2.3), so we also evaluated various pathways leading to the formation of N_2H_4. DFT reaction energies demonstrate that coupling of two NH_2^* species to form $N_2H_4^*$ has the lowest barrier (Table S6), and thus we restrict our analysis of N_2H_4 formation to this path. NO* can also react with nitrite to form N_2O*, which leads to N_2 production (i.e., the orange path in Scheme 2).[60,63] The detailed mechanism of N_2O* formation is not yet understood and will be the subject of future investigation. As N_2 formation was observed to be limited over Rh, we will not explore the N_2 formation pathway extensively in this work.

3.2. Rh and Pd Catalyst Behavior at Different pH Values. *3.2.1. Catalyst Structure.* The catalyst structures were characterized using TEM, XRD, CO chemisorption, and N_2 adsorption (Table 1). The alumina support had a nanorod morphology of ∼40 nm in length and ∼10 nm in width, with Rh/Al_2O_3 showing more agglomeration than Pd/Al_2O_3 (Figure S7). There were no discernible XRD peaks for the metals, indicating high dispersion of the 1 wt% metal. The detected diffraction peaks were those of the γ-Al_2O_3 phase (Figure S8). The N_2 isotherms indicated that the catalysts had a similar porous structure and an average pore size (Figure S9). On the basis of the metal particle sizes estimated from CO chemisorption and TEM analysis, the Rh metal is more dispersed on the alumina support than Pd.

3.2.2. Nitrite Reduction. Figure 1a shows the nitrite concentration versus time profiles of the Pd catalyst at different pH values. The Pd catalyst is highly active at acidic pH values, and the activity becomes lower with increasing pH, with the rate constant decreasing by over 99% from pH 4 to pH 11.5 (Figure 1c). These normalized rate constants are generally consistent with previous reports for Pd/Al_2O_3 where CO_2 is used as a buffer (pH ≈ 5.5).[64] The 92% decrease in activity from pH 4 to pH 8.5 is also in alignment with the

DOI: 10.1021/acscatal.9b03239
ACS Catal. 2020, 10, 494−509

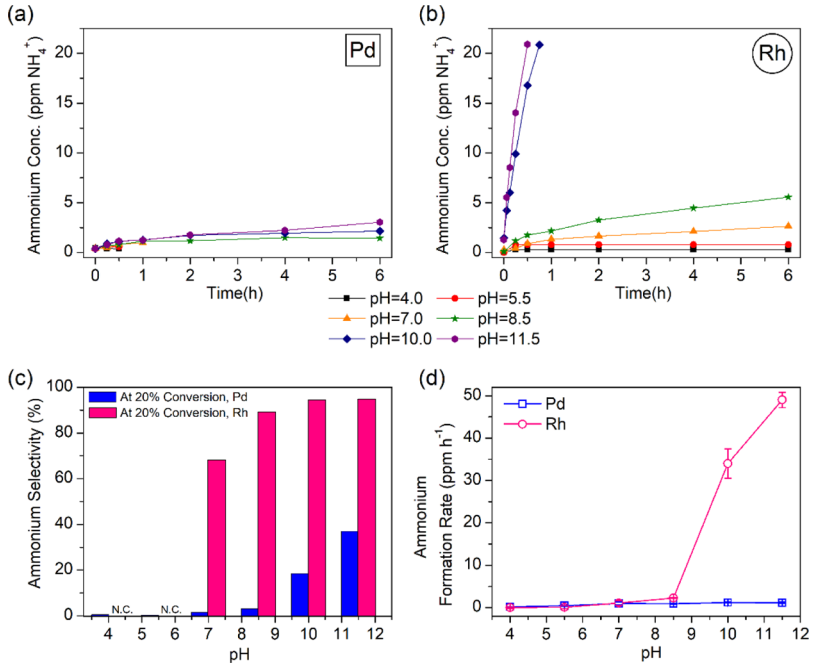

Figure 2. (a,b) Ammonium concentration vs time during the nitrite reduction reaction with 1 wt % Pd/Al_2O_3 and Rh/Al_2O_3 catalysts at different initial pH values. (c) Ammonium selectivity for 1 wt % Pd/Al_2O_3 and Rh/Al_2O_3 catalysts at 20% nitrite conversion at different initial pH values (N.C. = not calculated due to low activity). (d) Initial ammonium formation rate during the first hour of nitrite reduction reaction, with 1 wt % Pd/Al_2O_3 and Rh/Al_2O_3 catalysts at different initial pH values.

~80% decrease in activity from pH 4 to pH 8 in the initial reports by Vorlop and Tacke.[15]

Rh/Al_2O_3 showed very low activity at low pH, with metal-normalized rate constants consistent with the published results for Rh/Al_2O_3 at pH 6.[15] Counterintuitively, the Rh catalyst became active at high pH, in contrast to Pd (Figure 1b). Although Rh at pH 10 and 11.5 was much less active than Pd at pH 4, this observation updates the viewpoint that nitrite reduction catalysis needs an acidic environment to proceed.

Figure 1c shows a comparison of k_{cat} (normalized to the surface metal content) for Pd and Rh as a function of pH. The Rh catalyst was not active under acidic conditions where Pd catalysts were highly active, but these two catalysts showed similar initial activity at pH 8.5, with the activity crossover point occurring between pH 8.5 and 10. Although there have been no studies that describe the pH effects on Rh-catalyzed NO_2^- reduction, Werth and Strathmann groups reported on NO_3^- reduction over monometallic Rh.[25] They found that Rh became the most active at pH 3 and showed essentially no activity at pH 10. For NO_3^- reduction, the initial reduction step over Rh likely involves oxidation of the Rh surface, with subsequent reduction of NO_2^- surface species by the same active site. This two-step reduction pathway would be similar to that of the bimetallic Pd-based systems, in which the promoter metal (e.g., In, Cu, and Sn) reduces NO_3^-, and Pd serves to reduce the NO_2^- surface species (and to re-reduce the oxidized promoter metal via hydrogen spillover).[65−67] We hypothesize that the basic reaction media could promote oxidation of the Rh surface, making it unable to carry out the initial $NO_3^- \rightarrow NO_2^-$ reduction step but still able to carry out NO_2^- reduction.

The effect of basic pH on the nitrite reduction rate for each metal can also be investigated by running the reaction unbuffered. The nitrite reduction generates hydroxide anions (Scheme 1), which suggests that Pd (or Rh) catalytic activity should decrease (or increase) over time if the reaction medium is not buffered. Indeed, the Pd catalyst is deactivated after 6 h of reaction time when tested in DI water (initial pH of 6.5), and the nitrite concentration did not decrease any further after 1 day (final pH of 11.4) (Figure S1). It is generally accepted that the deactivation of Pd catalysts is due, in part, to the poisoning effect of hydroxyl groups generated during the reaction.[11,12,64,68] In comparison, the Rh catalyst rapidly removed nitrite anions to nondetectible levels within ~2 h under unbuffered conditions (initial and final pH values were 6.6 and 10.9, respectively). The pseudo-first-order rate constant was 8.9 L/g-surface-metal/min, which is ~10 times higher than the buffered cases (0.9 L/g-surface-metal/min, pH 7), indicating the promotional effect of the basic reaction medium on nitrite reduction over Rh. The mechanistic origin of this phenomena is investigated using DFT in Section 3.3.

3.2.3. Ammonium Formation. Ammonium is a byproduct in the nitrite reduction reaction. Figure 2a shows that the absolute concentration of ammonium formed over Pd was low; less than 5 ppm was formed after 6 h for all conditions tested. Ammonium selectivity (at 20% NO_2^- conversion) was <1% below pH 7, increasing to as high as 37% at pH 11.5 (Figure 2c). Both the total ammonium concentration and selectivity increased with increasing pH for the Pd catalyst, reinforcing observations that a high pH favors ammonium formation.[15,23] Ammonium selectivities were relatively constant at NO_2^- conversions above 20% (Figure S10). In addition to pH, ammonium selectivity over Pd is known to be a function of H_2 concentration in solution, indicating that the surface coverages of both N-containing surface species and H adatoms are important to determine the final products of nitrite reduction.[69]

Rh produced significantly more ammonium than Pd, except under acidic conditions where Rh catalysts were marginally active (Figure 2b). For Rh, the ammonium selectivity (at 20%

DOI: 10.1021/acscatal.9b03239
ACS Catal. 2020, 10, 494−509

NO_2^- conversion) was 68% at pH 7, increasing to 95% at pH 11.5 (Figure 2c). At higher NO_2^- conversions, the ammonium selectivity values over Rh were unchanged regardless of pH, reaching close to 90% under all neutral and basic pH conditions tested and >95% at the highest conversions measured (Figure S10). We observed a clear pH effect on NH_4^+ selectivity, and the observation of Rh reducing NO_2^- principally to NH_4^+ is consistent with the majority of the literature on nitrite (or nitrate) reduction over supported monometallic Rh.[14,15,66,70] Figure 2d shows the ammonium formation rates over the Rh and Pd catalysts in the pH range tested. The formation rates were comparable at pH 7 and below, but the rate increased much more over the Rh catalyst than Pd at pH > 7. The rapid ammonium formation rates for Rh (~40 times faster than that for Pd at pH 11.5) have implications in nutrient recovery from nitrate/nitrite wastewater.

3.2.4. Hydrazine Formation. Hydrazine (N_2H_4) is a known intermediate in the oxidation of ammonia to dinitrogen on both metal and metal oxide surfaces, particularly under conditions where there is limited oxygen available.[71,72] It can theoretically be generated from nitrite reduction with H_2 (Scheme 3). It has been speculated to be a potential intermediate in nitrite reduction reaction, but, to our knowledge, it has never actually been detected.[17]

Scheme 3. Nitrite Reduction to a Third Reaction Product, Hydrazine (with Free Energy Values at 25 °C, 1 M Reactant Concentrations, 1 atm)

$$2NO_2^- + 5H_2 \rightarrow N_2H_4 + 2H_2O + 2OH^- \quad \Delta G^\ominus = -515 \text{ kJ mol}^{-1}$$

In our reactions, hydrazine was detected in the bulk over the Pd catalyst at pH ≥ 7 (Figure 3). The overall quantity of hydrazine formed over Pd increases as a function of pH, with a maximum observed concentration of 0.5 ppm N_2H_4 at pH 11.5 (Figure 3a). In all cases where hydrazine is observed on Pd, its concentration decreases as the reaction proceeds. Figure 3c shows that the selectivity toward hydrazine increases monotonically with pH for Pd/Al_2O_3, which is expected based on its similarity to NH_4^+. This indicates that their surface formation mechanisms might be similar.

Hydrazine was detected at all pH values over Rh, also mirroring ammonium formation conditions. The total quantity and selectivity toward hydrazine were higher over Rh than those over Pd under almost all pH conditions tested, with a maximum observed concentration of 1.1 ppm N_2H_4 at pH 8.5. Whereas the hydrazine concentration strictly decreased over time for Pd, Figure 3b shows that the peak hydrazine concentration detected for Rh/Al_2O_3 moves to shorter times as the pH increases, with only pH 10 and pH 11.5 showing peak hydrazine concentrations at the beginning of the reaction. This strongly suggests that hydrazine behaves as a transient intermediate in the reduction process, decomposing as the reaction proceeds. This is also supported by the plot of hydrazine selectivity versus nitrite conversion for both catalysts, where the selectivity to hydrazine sharply decreased with nitrite conversion (Figure S11).

Both the hydrazine selectivity (Figure 3c) and the maximum observed hydrazine concentration (Figure 3b) display a volcano-shaped behavior as a function of the pH, peaking at pH 8.5. We attribute this trend in the hydrazine selectivity over Rh/Al_2O_3 to competitive formation between NH_3 and N_2H_4, which is governed by the hydrogen concentration on the surface. Hydrazine formation as a function of pH is investigated further using DFT microkinetic modeling in Section 3.3.2. Hydrazine is known to be an unstable intermediate that is readily decomposed over Rh, and additional experiments also confirmed that it is degraded much more rapidly over Rh than over Pd at pH 10 under

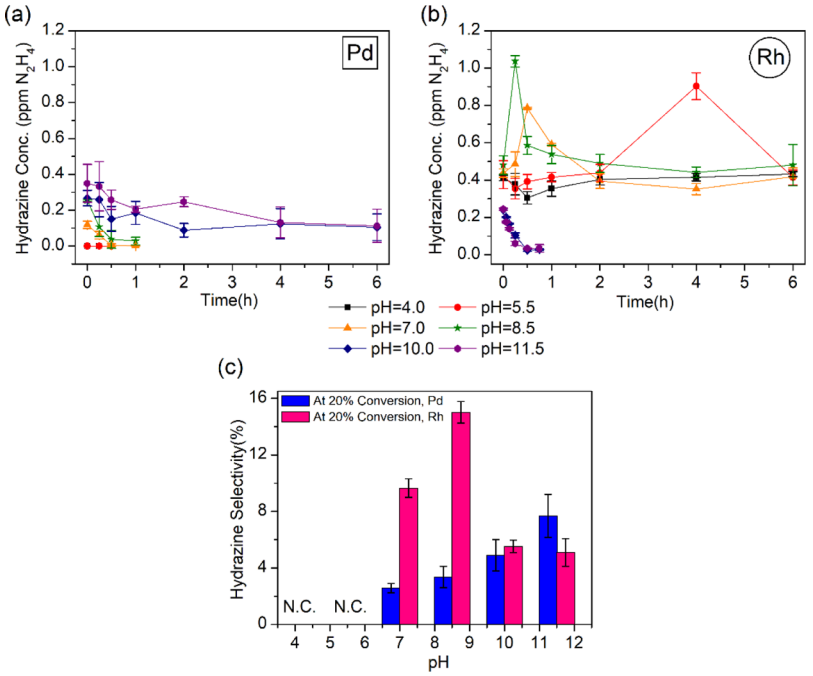

Figure 3. (a,b) Hydrazine selectivity versus nitrite conversion during the nitrite reduction reaction with 1 wt % Pd/Al_2O_3 and Rh/Al_2O_3 catalysts at different initial pH values. (c) Selectivity of hydrazine at 20% nitrite conversion [N.C. = not calculated due to low concentration (Pd) or low activity (Rh)].

DOI: 10.1021/acscatal.9b03239
ACS Catal. 2020, 10, 494−509

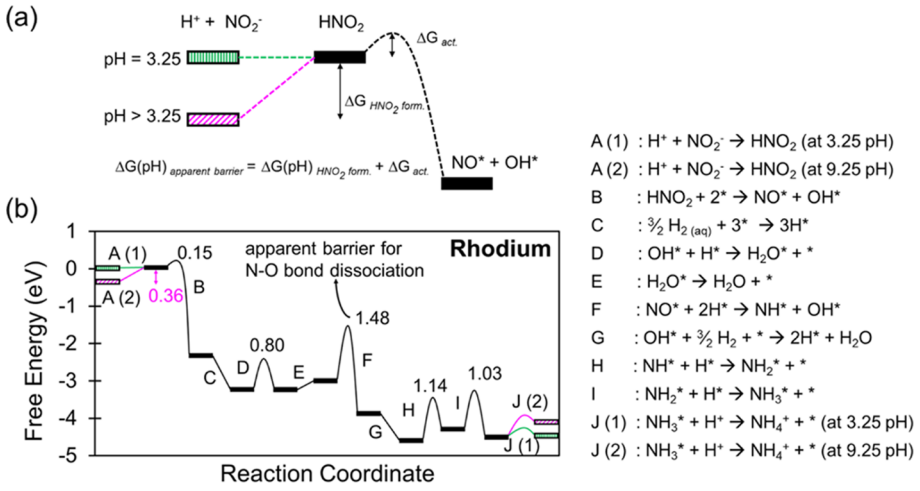

Figure 4. (a) NO_2^- adsorption and dissociation energetics with increasing pH. (b) Reaction energy diagram showing the reduction of NO_2^- + $2H^+$ + $3H_2$ → NH_4^+ + $2H_2O$ at T = 300 K, pH = 3.25, $P[H_2]$ = 1 atm, $[NO_2^-]$ = 50 ppm, and $[NH_3]$ = 2.5 ppm over Rh(111). Black markers and curves represent pH-independent reactions, and green and pink colors represent pH-dependent reactions at pH 3.25 and pH 9.25, respectively. Reaction energies and barriers involving the dissociation or association of surface reactants are computed relative to the energies of the reactant and product species in separate simulation cells at infinite separation (e.g., barrier D is computed as $\Delta G_{act} = G_{TS:H-OH^*} + G_* - G_{OH^*} - G_{H^*}$).

similar buffered, hydrogen-saturated conditions (Figures S12 and S13).

3.2.5. Implication of Hydrazine Formation. Hydrazine can be thought of as an additional source of N_2 and NH_4^+. Its decomposition has been highly studied for H_2 storage and generation for fuel cell applications. In water, the generation of hydrogen from hydrous hydrazine is accomplished through its complete decomposition (N_2H_4 → N_2 + $2H_2$), whereas ammonia is generated from the incomplete decomposition pathway ($3N_2H_4$ → $4NH_3$ + N_2).

Rh(0) nanoparticles are among the materials that have been highly investigated for room temperature H_2 generation from N_2H_4 in water. Singh et al. found that monometallic Rh shows ∼44% selectivity for the complete decomposition pathway compared to the incomplete decomposition pathway, under ambient conditions. Pd, on the other hand, was found to be inactive for N_2H_4 decomposition to H_2, although the N_2H_4 conversion was unreported.[73]

In our case, the reactor was saturated with hydrogen, and the competition between N-species coupling to N_2 and NH_x^* hydrogenation to NH_3^* is shifted by the increased presence of hydrogen atoms on the surface, increasing the observed selectivity toward NH_3. To explore hydrazine decomposition under simulated nitrite reduction conditions, 1.2 ppm hydrazine was injected into a hydrogen-saturated batch reactor buffered at pH 10 (near the maximum detected concentration during nitrite reduction). As mentioned previously, this confirmed that hydrazine can be decomposed/hydrogenated over the alumina-supported Pd and Rh catalysts under our experimental conditions. Under these conditions, Pd showed lower overall activity than Rh for hydrazine decomposition/hydrogenation (Figure S12). Although N_2H_4 shows an interference interaction with Nessler's reagent, the ammonium selectivity for both catalysts can be directly calculated after full conversion of N_2H_4. Rh displayed ∼100% selectivity to NH_4^+ after complete conversion. In comparison, Pd showed NH_4^+ selectivity of ∼35%. These results indicate that the formation and incomplete decomposition of hydrazine could play a significant role in the minor quantities of NH_4^+ observed with Pd.

When a higher initial concentration of hydrazine is used (5 mg/L), Pd becomes deactivated, whereas the reaction remains rapid over Rh (Figure S13). This could indicate that some intermediate of N_2H_4 decomposition poisons the Pd surface, which we hypothesize to be atomic nitrogen. This species has been observed to poison Pd during ammonia adsorption[74] and has been speculated to be largely unreactive during nitrite reduction when the reaction is near complete conversion.[75] The observation of this species during N_2H_4 reduction conditions via SERS will be discussed further in Section 3.4. At the higher initial concentration, the selectivity toward NH_4^+ remained at ∼100 and ∼35% for Rh and Pd, respectively. To the best of our knowledge, this is the first time that hydrazine formation and decomposition have been observed and quantified for the nitrate/nitrite reduction reaction.

This reaction pathway has mechanistic implications for hydrogen-generation applications, as the hydrogen-saturated conditions in our study are similar to the reaction conditions of hydrazine decomposition where the conversion is approaching 100%. Furthermore, the formation of N−N coupled species other than N_2 on metal surfaces under ambient aqueous conditions shows promise for the possibility of new avenues for nitrogen chemical transformations. Recently, researchers in the field of nitrogen chemistry have placed a larger focus on the development of more sustainable and efficient catalytic processes to minimize the use of fossil fuels needed for nitrogen transformation reactions.[76] Further study on the hydrazine formation pathway in the mechanism of nitrite reduction could enable synthesis of fine chemicals from nitrate and nitrite wastes.

3.3. DFT Calculations. *3.3.1. pH-Controlled NO_2^- Adsorption and Reduction to NH_4^+.* In this section, we report the DFT analysis of NO_2^- reduction mechanisms over Rh, where we focused on answering two questions

(1) Why does the NO_2^- reduction rate increase as the solution pH is increased?
(2) Why does the N_2H_4 production rate exhibit a volcano-like dependence on pH?

We first explored the effect of solution pH by considering its effect on the initial adsorption and dissociation of nitrite in

DOI: 10.1021/acscatal.9b03239
ACS Catal. 2020, 10, 494−509

varying protonation states (Figure 4a). The protonation state of the nitrite anion will be controlled by the solution pH, where HNO_2 will be the dominant species below pH = 3.25 (i.e., the pKa of HNO_2) and NO_2^- will be the dominant species above pH = 3.25.[55] Thus, we considered the adsorption and dissociation of both HNO_2 and NO_2^- in our analysis. We found that HNO_2 rapidly dissociates to form NO* and OH*, where NEB calculations confirmed that there is no barrier for HNO_2 dissociation on the 0 K potential energy surface (Figure S5) over Rh(111). The free energy barrier ΔG_{act} = 0.15 eV shown in Figure 4a is derived from the loss of translational entropy as the molecule approaches the surface. This corresponds to the HNO_2 dissociation barrier when the solution is at or below pH 3.25, where there is no free energy "penalty" to form the HNO_2 molecule.

Above pH = 3.25, we computed the apparent HNO_2 dissociation barrier by accounting for the free energy required to form the HNO_2 molecule by protonating NO_2^-, which increases the apparent barrier for HNO_2 dissociation because there is an uphill energy penalty to form HNO_2 above pH = 3.25. As such, the apparent barrier for HNO_2 adsorption is pH-dependent and increases as the solution pH increases. We also considered the adsorption and dissociation of NO_2^-, which is pH-independent above pH = 3.25, where the molecule adsorbs as NO_2^* and then dissociates on the surface to form NO* and O*.

As seen in the DFT reaction free energy diagram shown in Figure 4b, HNO_2 dissociation to NO* and OH* over Rh is highly favorable (i.e., ΔG_{rxn} = −2.32 eV and ΔG_{act} = 0.15 eV at pH = 3.25). We inferred from this reaction energy diagram that the catalyst surface may be easily poisoned by NO*, as NO* will be rapidly deposited on the surface via HNO_2 dissociation. We evaluated the formation of NH* from NO* through three different pathways: NO* dissociation, HNO* formation, and NOH* formation.[77,78] Sequential NO* hydrogenation to HNO* and HNOH* followed by dissociation to NH* and OH* is the preferred pathway for NH* formation on Rh, as this pathway has a smoother potential energy surface compared to alternative paths leading to NH* (Figure S14). The apparent barrier to dissociate NO* to form NH* is found to be 1.48 eV on Rh, which suggests that NO* dissociation will be slow. This further indicates that NO* poisoning over Rh will play an important role in the overall kinetics, as NO* is quickly deposited on the surface and is slowly removed from the surface.

The reaction energy diagram suggests that rapid HNO_2 dissociation is promoted at low pH, and when coupled with slow NO* dissociation and hydrogenation, this leads to NO* poisoning. Since the apparent barrier for HNO_2 formation and dissociation increases with increasing pH, we propose that increasing the solution pH effectively suppresses NO* surface poisoning by slowing down the rate at which NO* is deposited on the surface. This possibility will be explored in the following section, where a microkinetic model is employed to explore the connections between pH, reaction rates, and surface coverage. In comparison, when we evaluated the NH_3 formation pathway over Pd, we found an apparent barrier of 2.08 eV for NO* to form NH* (Figures S15 and S16), which is consistent with previous reports.[79,80] The high NO* dissociation barrier over Pd explains its significantly reduced selectivity toward NH_3.

3.3.2. Microkinetic Model. We performed a microkinetic modelling analysis of NO_2^- reduction to understand the changes in NH_3/NH_4^+ and N_2H_4 formation rates over the Rh surface as a function of pH. We did not include a reaction path leading to N_2 formation in this model (i.e., reactions R22-R24 in Scheme 2) because Rh is not observed experimentally to be selective toward N_2 formation. In this model, the solution pH only impacts reaction rates and energies by determining the relative free energy of HNO_2/NO_2^- and NH_3/NH_4^+ molecules (i.e., pH only affects reaction steps involving a proton, which are shown in green and pink in Figure 4b). All reactions, reaction energies, and reaction barriers used to build the microkinetic model are reported in Tables S4 and S5. Figure 5a,b shows the results of the microkinetic model at varying pH,

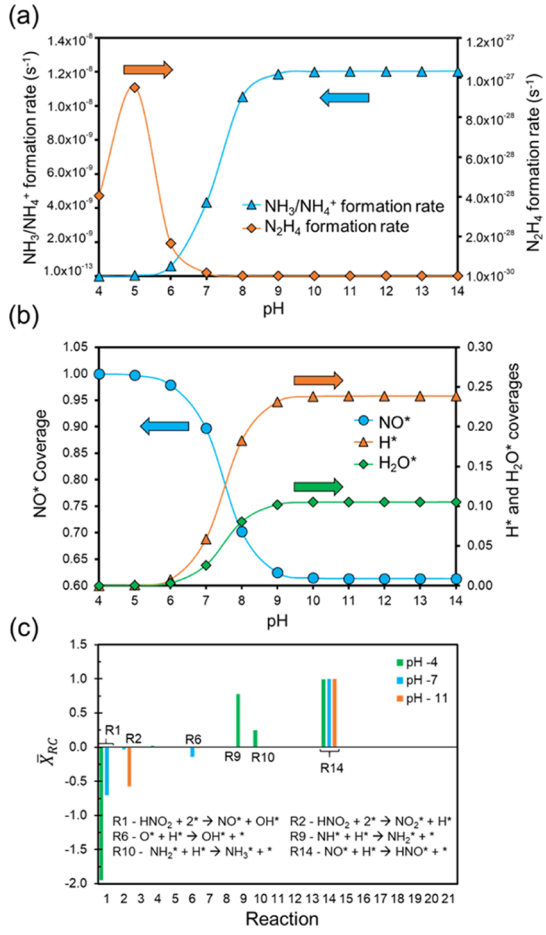

Figure 5. Microkinetic model showing (a) NH_3/NH_4^+ (blue) and N_2H_4 (orange) formation rates and (b) NO*, H*, and H_2O* surface coverages at varying pH values and at 300 K after a time elapse of 10^5 s. (c) Degree of transient rate control ($\bar{X}_{RC}$) at pH 4, 7 and 11.

which demonstrates that the NH_3/NH_4^+ formation rate increases and NO* surface coverage decreases with increasing pH on the Rh(111) surface. This can be attributed to the increasing barrier for HNO_2 adsorption, which mitigates NO* build-up on the surface. It should be noted that the NO_2^- reduction rate and surface coverages are transient in nature, and the data shown in Figure 5 corresponds to the state of the catalyst surface after 10^5 s have elapsed (starting with an empty surface). The full reaction transients are shown in Figure S18, where we see that initially the reaction rate is higher at low pH before the surface becomes poisoned with NO*, which would be intuitive for a reaction that consumes protons in the absence of any surface-poisoning effects. This trend reverses as the surface approaches steady state, as NO* builds up on the

DOI: 10.1021/acscatal.9b03239
ACS Catal. 2020, 10, 494−509

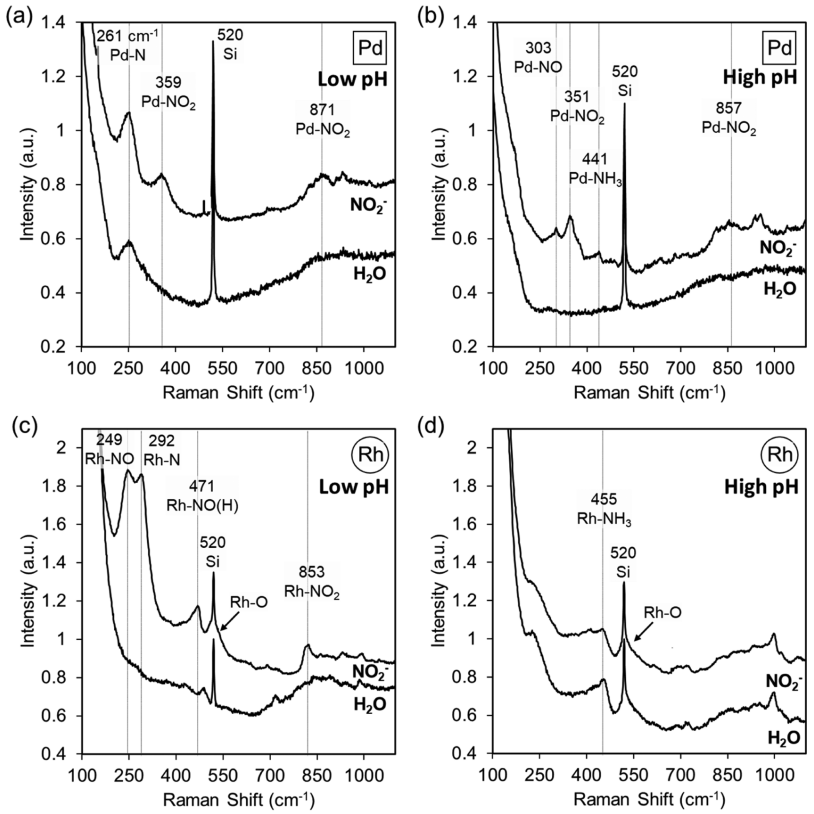

Figure 6. Accumulated SER spectra over metal-plated Au NSs of solutions containing 5 ppm NO_2^- and water background for (a,b) Pd plating at low and high pH and (c,d) Rh plating at low and high pH. Low pH = 3.1. High pH = 9.4.

surface and inhibits further reaction. The computational rates predicted by the model are much lower than those observed in the experiments because our model employs the least reactive (111) facet, as discussed above in the Computational Methodology section. Consequently, the timescales required to reach steady state are much longer than those observed experimentally, as seen in Figure S18. Thus, we restrict our analysis of these models to only qualitative trends that can yield mechanistic insight and do not rely on quantitative comparisons to the experiment.

The model shows that increasing the HNO_2 dissociation barrier mitigates the NO* poisoning effect, which is evident in the increased NH_3/NH_4^+ formation rate predicted at high pH. The decrease in NO* coverage is coupled with an increase in H* coverage (Figure 5b) because here we assume that excess H_2 is available (i.e., in the experiments the system was presaturated with hydrogen). The rate plateau at pH ≈ 9 in Figure 5a can be understood by noting that the barrier for dissociative HNO_2 adsorption is pH-dependent and increases with pH (i.e., pH controls the free energy of NO_2^- protonation to form HNO_2), whereas the barrier for direct NO_2^- adsorption/dissociation is pH-independent. The crossover of these activation barriers occurs at pH ≈ 9, where the overall reaction rate becomes insensitive to pH because direct NO_2^- adsorption becomes energetically favored at pH > 9. The position of the rapid jump in rate followed by a plateau is in good agreement with the experimentally observed increase in rate between pH ∼5 and ∼10, given the accuracy of our DFT calculations (i.e., ±2 pH units correspond to ±0.12 eV at 300 K). We also computed NO* adsorption energies with varying OH* coverage to determine if adsorbate−adsorbate interactions could also explain the observed pH effect (Table S7). We found that the NO* adsorption energy varied only slightly with varying OH* coverage (i.e., by ∼0.2 eV), and therefore, we conclude that the primary effect of changing the solution pH is to change the availability of protonated nitrite.

The formation of N_2H_4 was also evaluated using the microkinetic model, which demonstrates that peak N_2H_4 formation occurs at pH ≈ 5 just prior to the takeoff in NH_3 formation. This suggests that there is a competition between NH_2^* coupling (i.e., $NH_2^* + NH_2^* \rightarrow N_2H_4^*$) and hydrogenation (i.e., $NH_2^* + H^* \rightarrow NH_3^*$) that determines the selectivity of the reaction. At low pH, both reactions are poisoned by high NO* coverage and exhibit low rates. As the pH increases, surface sites become available that enable NO* dissociation, but the surface is not yet covered with a substantial amount of H*, which in turn allows NH_2^* coupling reactions to form N_2H_4. As the pH increases further, there is a clear increase in the H* coverage, which tips the balance toward NH_3^* production. Thus, we see that the N_2H_4 formation rate exhibits volcano-like dependence on the solution pH. Note that the N_2H_4 formation rate is always many orders of magnitude below the NH_3 formation rate, which is expected, given the energetically uphill nature of N_2H_4 formation compared to NH_3. Also, in our model, we considered only the Rh(111) facet, and thus we expect that Rh nanoparticles that expose metal atoms with varying topological environments (e.g., edges and steps) may be more favorable for N_2H_4 production. Indeed, He et al. have demonstrated computationally that N_2H_4 desorption becomes more favorable with decreasing Rh nanoparticle size,[81] leading to easier formation and desorption of N_2H_4.

Finally, we performed a degree of rate control analysis to further support our interpretation of the microkinetic model.

DOI: 10.1021/acscatal.9b03239
ACS Catal. 2020, 10, 494−509

Figure 5c shows that HNO_2 dissociation to NO* and OH* (reaction R1) has a large negative $\bar{X}_{RC}$ at low pH indicating the significant poisoning effect of this reaction. The magnitude of $\bar{X}_{RC}$ for R1 decreases as pH increases, which demonstrates that increasing the barrier for HNO_2 dissociation delays the onset of NO* surface poisoning. At higher pH, $\bar{X}_{RC}$ for R2 grows more negative indicating that NO* is derived from direct NO_2^- adsorption and dissociation under basic conditions. R9 and R10 (i.e., NH_3^* formation from NH*) have small but non-zero, $\bar{X}_{RC}$ values at low pH, which further demonstrates the rate-limiting nature of NH_3^* formation when the surface is poisoned. This confirms that at lower pH, NH_x species are slowly hydrogenated to NH_3^*, allowing for NH_2^* coupling to form N_2H_4. R14 (i.e., HNO* formation from NO*) has the largest positive $\bar{X}_{RC}$, which demonstrates that HNO* formation is the preferred path for N−O bond dissociation via the NO* + 2H* → NH* + OH* reaction.

Reaction R14 controls the rate at all pH values, which demonstrates that breaking the N−O bond in NO* is the essential step that determines the overall steady-state rate of NO_2^- reduction. Here, we are reporting a transient degree of rate control ($\bar{X}_{RC}$), which captures the cumulative effect of a barrier change at t = 0 s on the state of the surface and the corresponding rates at some later time of interest (e.g., at t = 10^5 s in this analysis). This differs from the instantaneous degree of rate control (X_{RC}),[58] and a more detailed discussion of $\bar{X}_{RC}$ versus X_{RC} is provided in the Supporting Information (Figures S17−S20).

3.4. SERS Evidence for Nitrogen Surface Species. Inspired by the stark differences in NO* coverage at varying pH predicted by the microkinetic model, we employed in aqua SERS to study and compare the adsorbed intermediates of the nitrite reduction reaction at low (∼3) and high (∼9) pH values (Figure 6). Pd was again used for comparison here because of our previous experience in the application of model Au@Pd NS catalysts for the in-situ investigation of transient reaction intermediates[36,37] as well as the existing literature on the pH-dependence of reaction intermediates on Pd during nitrite reduction.[23] In all of the experiments, a broad background was observed from 1000 to 1800 cm^{-1} typical of NS SERS experiments,[37,38] with broad peaks at 1000 and 1550 cm^{-1} typical of Si−O of the silicon wafer and carbonaceous residues.

A broad oxide peak centered at ∼540 cm^{-1} was apparent after the introduction of the N_2-saturated low pH solution (Figure S21a, 1−5 min), which is indicative of PdO formation.[82] The H_2-saturated low pH solution was introduced after 5 min and was effective at re-reducing Pd, as evidenced by the disappearance of the oxide peak (Figure S21a, 6−10 min). The low pH nitrite solution was introduced after 10 min and monitored over 10 min (i.e., scans 11−20). Figure 6a shows the normalized accumulated spectra of the nitrite-containing solution and the previous H_2-saturated solution (background). Upon the introduction of nitrite, a number of new bands appear. The band at 261 cm^{-1} is consistent with the Pd−N stretch of surface-bound atomic N.[75,83] Bands at 359 cm^{-1} (ν_{Pd-N}) and 870 cm^{-1} (NO_2^- deformation) and the broad feature at 1600 cm^{-1} (symmetric NO_2^- stretching) agree with surface-bound NO_2^-.[83,84]

High-pH, H_2-saturated water was introduced after 20 min of total reaction time, followed by the high-pH NO_2^- solution after 25 min. Figure 6b shows the normalized accumulated spectra from these high pH experiments. While surface NO_2^- likely is still on the surface (bands at 351$^-$ and 857 cm^{-1} and increase in broad feature ∼1600 cm^{-1}), species not found in the low pH conditions are also apparent. The low-frequency mode at 303 cm^{-1} is consistent with the Pd−N stretch of surface-bound NO.[84,85] The emergence of the small peak at 441 cm^{-1} may be due to the formation of trace amounts of ammonium from H_2 left over from the H_2 treatment.[74] Finally, we observe small modes at ∼1954 and 2102 cm^{-1}, which may be related to bridging and terminally bound N_2O species (Figure S21c).[85,86]

The SERS experiment was performed analogously using the Rh-plated Au NSs. Similar to the Pd case, a broad oxide peak centered at ∼520 cm^{-1} was apparent after the introduction of the N_2-saturated low pH solution (Figure S22a, 1−5 min).[82] The H_2-saturated low pH solution was introduced after 5 min and was effective at re-reducing the Rh, as evidenced by the disappearance of the oxide peak (Figure S22a, 6−10 min). The low pH nitrite solution was introduced after 10 min and monitored for 10 min. Figure 6c shows the normalized accumulated spectra of the nitrite-containing solution and the previous H_2-saturated solution (background). We attribute the band at 292 cm^{-1} to the Rh−N stretch of surface-bound atomic N,[87] while we tentatively assign the band at 249 cm^{-1} to the Rh−N stretch of surface-bound NO adsorbed in a linear fashion (e.g., the fcc or atop position). This assignment is based on the observation of similar red shifts for the adsorption of NO compared to atomic N on both Pd and Pt in SERS[85] as well as from the vibrational frequencies we calculated using DFT on the Rh(111) surface, which also show a red-shifted frequency of NO compared to N (Table S8). Molecularly adsorbed NO has also been observed on Rh(111) in acidic solutions of nitrite using in situ Fourier transform infrared (FTIR) spectroscopy, and thus we also expect to observe it under these very similar conditions.[88]

The small feature at 471 cm^{-1} may be due to the Rh−N stretch of surface-bound NOH formed by reaction of the NO species with H_2,[89] or it could also correspond to the N−O bending mode of adsorbed NO in the atop position.[90] Surface-bound NH_3 has been ruled out in this case because of the much higher intensity of the feature compared to control experiments of direct NH_3 adsorption onto the metal NSs (Figure S23) as well as the negligible NH_3 formation rate observed at pH 4 in our catalytic experiments (Figure 2). Finally, the bands at 853 cm^{-1} and the broad band at 1600 cm^{-1} are consistent with surface-bound NO_2. The shoulder around the Si peak at 520 cm^{-1} suggests that the Rh surface was partially oxidized by the nitrite. A very faint feature ∼2100 cm^{-1} is consistent with the trace formation of N_2O (Figure S21b).[85,86]

In contrast, much fewer adsorbates were observed during the high pH experiments (Figure 6d). A slight increase in the bands ∼853 and ∼1600 cm^{-1} suggest that there still may be some surface-bound NO_2.[87] The trace feature at ∼455 cm^{-1} may be related to surface-bound ammonium. In the case of Pd, the peaks observed in our SERS experiments can be compared to those from the Lefferts group using attenuated total reflectance infrared (ATR-IR) spectroscopy.[23] For Pd, NO is not observed at low pH, which suggests that the reaction happens quickly under these conditions. This is further supported by the observation of adsorbed atomic N, which is hypothesized to be formed when the reaction is near complete conversion and to react very slowly with hydrogen to form ammonia.[75] Adsorbed N_2O is not observed at low pH, likely due to the rapid reduction of N_2O to N_2 that has been

DOI: 10.1021/acscatal.9b03239
ACS Catal. 2020, 10, 494−509

observed for Pd.[91] At high pH, the observation of NO indicates that the reaction proceeds much more slowly under these conditions, which is well-known in the literature and expected based on the results presented in Figure 1. Combined with the lack of features observed for atomic N, this also supports the notion that N−O bond dissociation is extremely slow under basic conditions over Pd. The observation of trace N_2O on Pd suggests that the formation of N_2 also proceeds much more slowly under these conditions and supports our hypothesis that the NO surface coverage is low, as NO and N_2O are known to be competitively adsorbed with NO adsorption being known to prevent N_2O adsorption and dissociation to N_2.[83] The lack of a peak corresponding to atomic N along with the observation of NH_3 at high pH strongly suggests that the H coverage is high under these conditions. Interestingly, N_2O was not observed by the Lefferts group at pH 9 over Pd, whereas it could be observed in small amounts over Pt.[23] However, this is probably due to the increased sensitivity of SERS for measuring ultralow concentrations of bound molecules when compared to ATR-FTIR techniques.[92]

For Rh, NO is observed at low pH, supporting the notion that NO dissociation is hindered under acidic conditions because of the lack of available surface sites (from rapid NO_2^- dissociation). The preponderance of features corresponding to NO/NOH and atomic N observed in the SERS experiments over Rh suggest that the Rh surface has a high surface coverage of these more unreactive N-species, which is consistent with the surface coverages calculated by our microkinetic model (Figure 5b). Conversely, this implies that the hydrogen surface coverage is low,[93] and the subsequent ammonium formation rates (through hydrogenation of atomic N) will also be low, consistent with our experimental results. Furthermore, the observation of trace quantities of N_2O indicates that the N_2 formation pathway can proceed over Rh, albeit very slowly. At high pH, the lack of a peak corresponding to adsorbed NO supports our conclusion that the NO surface coverage should be low under these conditions because of the fact that NO_2^- dissociation is slowed allowing for rapid N−O bond dissociation. Furthermore, the observation of NH_3 without a feature corresponding to atomic N indicates that hydrogenation to NH_3 is rapid under these conditions, consistent with the ammonium formation rates observed in our experiments at pH > 8.5 (Figure 2d).

Last, we note that features corresponding to adsorbed hydrazine were not detected in any of the experiments in Figure 6 or in control experiments at significantly increased concentration (~500 mg N_2H_4/L), consistent with the reported literature on hydrazine detection via SERS.[94] Control experiments at 10 mg N_2H_4/L were performed analogously to the "high pH" conditions in Figure 6 (Figure S24). The resulting spectra of the Au@Pd NS showed a weak feature at ~290 cm^{-1}, which could suggest the formation of atomic N from N_2H_4, consistent with the catalytic results discussed in Section 3.2.4. The spectra for the Au@Rh NS appears to be consistent with the experimental results, with small features at ~300 and ~420 cm^{-1} suggesting both atomic N and NH_3 formation.

In summary, our observations using SERS corroborate the notion that the NO* surface coverage during nitrite reduction helps to determine the activity of precious metal catalysts. Adsorbed atomic N, a speculated unreactive intermediate for Pd, has been observed during nitrite reduction conditions, as well as bound N_2O, confirming the hypotheses deduced from previous FTIR experiments.[23,75] Furthermore, the presence or absence of NO on both metals at high and low pH serves to validate our analysis of nitrite adsorption energetics as a function of pH for both Pd and Rh as well as the more in-depth surface coverage analysis done using the microkinetic model for Rh.

4. CONCLUSIONS

In this work, Rh supported on alumina was tested for its activity in the nitrite reduction reaction over a range of pH conditions. As a control, this behavior was benchmarked against a Pd on alumina catalyst which was active toward nitrite reduction at low pH values and exhibited a decreasing trend in activity as the pH increased. Pd was found to show selectivity predominantly to dinitrogen, with traces of ammonium and hydrazine observed at higher pH values. In contrast, the Rh catalyst was inactive at low pH but became active at higher pH values. The selectivity of Rh was primarily to ammonium, with small quantities of hydrazine formed as well.

Experimental observations and DFT calculations demonstrated that nitrite reduction over Rh is strongly impacted by NO* surface poisoning and that this poisoning effect is controlled by solution pH through the rate of dissociative HNO_2 adsorption. This prediction was corroborated by the experimental SERS analysis, which shows that the Rh surface is indeed covered with NO* at low pH. The microkinetic model also demonstrated that the competition between NH_3 and N_2H_4 formation is regulated by the hydrogen surface coverage, which is also influenced by the pH of the solution. While the NO/H surface ratio has long been hypothesized to be the crucial parameter in determining the nitrite reduction activity and selectivity over Pd (affected by the NO_2^- concentration, NO_2^- conversion, and the H_2 flow rate/reductant concentration), our work demonstrates that the surface NO/H ratio is also modulated by the pH of the reaction medium through the relative abundance of protonated and deprotonated nitrite, which changes the barrier for nitrite dissociation to NO*. Typically, the adsorption of NO_2^- as a function of pH is only considered from an electrostatic point of view; however, we have shown using DFT that the acid dissociation equilibrium of NO_2^- also plays a significant role in the energetics of the nitrite reduction reaction.

This study expands the frontiers of the catalytic nitrite reduction process and has provided initial insight into the aqueous nitrogen reduction chemistry of other precious metals outside the scope of conditions which have been optimized for Pd. Additional fundamental investigation of denitrification reaction pathways presents an opportunity to develop technologies for the formation of fine chemical species through N−N coupling or the coupling of N-species with other heteroatoms or carbonaceous species present in real wastewater.

■ ASSOCIATED CONTENT

Supporting Information

The Supporting Information is available free of charge at https://pubs.acs.org/doi/10.1021/acscatal.9b03239.

DFT converged structures, microkinetic model code, and reaction energy calculations (ZIP)

DOI: 10.1021/acscatal.9b03239
ACS Catal. 2020, 10, 494−509

Experimental and computational details and additional data (PDF)

AUTHOR INFORMATION

Corresponding Authors

*E-mail: tsenftle@rice.edu (T.P.S.).
*E-mail: mswong@rice.edu (M.S.W.).

ORCID

Thomas P. Senftle: 0000-0002-5889-5009
Michael S. Wong: 0000-0002-3652-3378

Author Contributions

▽C.A.C., C.P.R., and H.X. contributed equally to this work.

Notes

The authors declare no competing financial interest.

ACKNOWLEDGMENTS

The authors gratefully acknowledge partial support from the NSF Nanosystems Engineering Research Center for Nanotechnology-Enabled Water Treatment (ERC-1449500). C.A.C. acknowledges support from the NSF Graduate Research Fellowship Program (DGE-1450681). G.L. and H.X. acknowledge support from the State Key Research and Development Project of China (2016YFB0301603). T.P.S. acknowledges the start-up funding support from the Rice University. Any opinions, findings, and conclusions or recommendations expressed in this material are those of the author(s) and do not necessarily reflect the views of the National Science Foundation.

REFERENCES

(1) Galloway, J. N.; Townsend, A. R.; Erisman, J. W.; Bekunda, M.; Cai, Z.; Freney, J. R.; Martinelli, L. A.; Seitzinger, S. P.; Sutton, M. A. Transformation of the Nitrogen Cycle: Recent Trends, Questions, and Potential Solutions. *Science* **2008**, *320*, 889−892.

(2) Stevens, C. J. Nitrogen in the Environment. *Science* **2019**, *363*, 578−580.

(3) Erisman, J. W.; Sutton, M. A.; Galloway, J.; Klimont, Z.; Winiwarter, W. How a Century of Ammonia Synthesis Changed the World. *Nat. Geosci.* **2008**, *1*, 636−639.

(4) *The European Nitrogen Assessment. Sources, Effects and Policy Perspectives*Sutton, M. A., Howard, C. M., Erisman, J. W., Billen, G., Bleeker, A., Grennfelt, P., van Grinsven, H., Grizzetti, B., Eds.; Cambridge University Press: Cambridge, 2011.

(5) US EPA. *Reactive Nitrogen in the United States: An Analysis of Inputs, Flows, Consequences, and Management Options. A Report of the EPA Science Advisory Board*, 2011.

(6) Miller, S. A.; Landis, A. E.; Theis, T. L. Use of Monte Carlo Analysis to Characterize Nitrogen Fluxes in Agroecosystems. *Environ. Sci. Technol.* **2006**, *40*, 2324−2332.

(7) Gulis, G.; Czompolyova, M.; Cerhan, J. R. An Ecologic Study of Nitrate in Municipal Drinking Water and Cancer Incidence in Trnava District, Slovakia. *Environ. Res.* **2002**, *88*, 182−187.

(8) Cantor, K. P. Drinking Water and Cancer. *Cancer Causes Control* **1997**, *8*, 292−308.

(9) Issenberg, P. Nitrite, Nitrosamines, and Cancer. *Fed. Proc.* **1976**, *35*, 1322−1326.

(10) Schullehner, J.; Hansen, B.; Thygesen, M.; Pedersen, C. B.; Sigsgaard, T. Nitrate in Drinking Water and Colorectal Cancer Risk: A Nationwide Population-Based Cohort Study. *Int. J. Cancer* **2018**, *143*, 73−79.

(11) Chaplin, B. P.; Reinhard, M.; Schneider, W. F.; Schüth, C.; Shapley, J. R.; Strathmann, T. J.; Werth, C. J. Critical Review of Pd-Based Catalytic Treatment of Priority Contaminants in Water. *Environ. Sci. Technol.* **2012**, *46*, 3655−3670.

(12) Martínez, J.; Ortiz, A.; Ortiz, I. State-of-the-Art and Perspectives of the Catalytic and Electrocatalytic Reduction of Aqueous Nitrates. *Appl. Catal., B* **2017**, *207*, 42−59.

(13) Vorlop, K.-D.; Tacke, T. Erste Schritte auf dem Weg zur edelmetallkatalysierten Nitrat- und Nitrit-Entfernung aus Trinkwasser. *Chem. Ing. Tech.* **1989**, *61*, 836−837.

(14) Hörold, S.; Vorlop, K.-D.; Tacke, T.; Sell, M. Development of Catalysts for a Selective Nitrate and Nitrite Removal from Drinking Water. *Catal. Today* **1993**, *17*, 21−30.

(15) Hörold, S.; Tacke, T.; Vorlop, K. D. Catalytical Removal of Nitrate and Nitrite from Drinking Water: 1. Screening for Hydrogenation Catalysts and Influence of Reaction Conditions on Activity and Selectivity. *Environ. Technol.* **1993**, *14*, 931−939.

(16) Epron, F.; Gauthard, F.; Barbier, J. Catalytic Reduction of Nitrate in Water on a Monometallic Pd/CeO2 Catalyst. *J. Catal.* **2002**, *206*, 363−367.

(17) Prüsse, U.; Vorlop, K.-D. Supported Bimetallic Palladium Catalysts for Water-Phase Nitrate Reduction. *J. Mol. Catal. A: Chem.* **2001**, *173*, 313−328.

(18) Guy, K. A.; Xu, H.; Yang, J. C.; Werth, C. J.; Shapley, J. R. Catalytic Nitrate and Nitrite Reduction with Pd−Cu/PVP Colloids in Water: Composition, Structure, and Reactivity Correlations. *J. Phys. Chem. C* **2009**, *113*, 8177−8185.

(19) Zhang, R.; Shuai, D.; Guy, K. A.; Shapley, J. R.; Strathmann, T. J.; Werth, C. J. Elucidation of Nitrate Reduction Mechanisms on a Pd-In Bimetallic Catalyst Using Isotope Labeled Nitrogen Species. *ChemCatChem* **2013**, *5*, 313−321.

(20) Soares, O. S. G. P.; Órfão, J. J. M.; Pereira, M. F. R. Activated Carbon Supported Metal Catalysts for Nitrate and Nitrite Reduction in Water. *Catal. Lett.* **2008**, *126*, 253−260.

(21) Prüsse, U.; Hähnlein, M.; Daum, J.; Vorlop, K.-D. Improving the Catalytic Nitrate Reduction. *Catal. Today* **2000**, *55*, 79−90.

(22) Guo, S.; Heck, K.; Kasiraju, S.; Qian, H.; Zhao, Z.; Grabow, L. C.; Miller, J. T.; Wong, M. S. Insights into Nitrate Reduction over Indium-Decorated Palladium Nanoparticle Catalysts. *ACS Catal.* **2018**, *8*, 503−515.

(23) Ebbesen, S. D.; Mojet, B. L.; Lefferts, L. Effect of pH on the Nitrite Hydrogenation Mechanism over Pd/Al2O3 and Pt/Al2O3: Details Obtained with ATR-IR Spectroscopy. *J. Phys. Chem. C* **2011**, *115*, 1186−1194.

(24) Huo, X.; Van Hoomissen, D. J.; Liu, J.; Vyas, S.; Strathmann, T. J. Hydrogenation of Aqueous Nitrate and Nitrite with Ruthenium Catalysts. *Appl. Catal., B* **2017**, *211*, 188−198.

(25) Chen, X.; Huo, X.; Liu, J.; Wang, Y.; Werth, C. J.; Strathmann, T. J. Exploring beyond Palladium: Catalytic Reduction of Aqueous Oxyanion Pollutants with Alternative Platinum Group Metals and New Mechanistic Implications. *Chem. Eng. J.* **2017**, *313*, 745−752.

(26) Neubrand, J. *Encyclopedia of Automotive Engineering*; Crolla, D., Foster, D. E., Kobayashi, T., Vaughan, N., Eds.; John Wiley & Sons, Ltd.: Chichester, UK, 2014.

(27) Lee, Y.; Jang, S.; Cho, C.-W.; Bae, J.-S.; Park, S.; Park, K. H. Recyclable Rhodium Nanoparticles: Green Hydrothermal Synthesis, Characterization, and Highly Catalytic Performance in Reduction of Nitroarenes. *J. Nanosci. Nanotechnol.* **2013**, *13*, 7477−7481.

(28) Yao, H.-C.; Emmett, P. H. Kinetics of Catalytic Liquid Phase Hydrogenation. I. The Hydrogenation of Aromatic Nitrocompounds over Colloidal Rhodium and Palladium. *J. Am. Chem. Soc.* **1959**, *81*, 4125−4132.

(29) Duca, M.; Koper, M. T. M. Powering Denitrification: The Perspectives of Electrocatalytic Nitrate Reduction. *Energy Environ. Sci.* **2012**, *5*, 9726.

(30) G Casella, I.; Contursi, M. Highly Dispersed Rhodium Particles on Multi-Walled Carbon Nanotubes for the Electrochemical Reduction of Nitrate and Nitrite Ions in Acid Medium. *Electrochim. Acta* **2014**, *138*, 447−453.

(31) Tucker, P. M.; Waite, M. J.; Hayden, B. E. Electrocatalytic Reduction of Nitrate on Activated Rhodium Electrode Surfaces. *J. Appl. Electrochem.* **2004**, *34*, 781−796.

DOI: 10.1021/acscatal.9b03239
ACS Catal. 2020, 10, 494−509

(32) Witońska, I.; Karski, S.; Gołuchowska, J. Kinetic Studies on the Hydrogenation of Nitrate in Water Using Rh/Al2O3 and Rh-Cu/Al2O3 Catalysts. *Kinet. Catal.* **2007**, *48*, 823−828.
(33) Primet, M. Infrared Study of CO Chemisorption on Zeolite and Alumina Supported Rhodium. *J. Chem. Soc., Faraday Trans. 1* **1978**, *74*, 2570−2580.
(34) Boitiaux, J. P.; Cosyns, J.; Vasudevan, S. Preparation and Characterisation of Highly Dispersed Palladium Catalysts on Low Surface Alumina, Their Notable Effects in Hydrogenation. *Stud. Surf. Sci. Catal.* **1983**, *16*, 123.
(35) Sheu, L. L.; Karpinski, Z.; Sachtler, W. M. H. Effects of Palladium Particle Size and Palladium Silicide Formation on Fourier Transform Infrared Spectra and Carbon Monoxide Adsorbed on Palladium/Silicon Dioxide Catalysts. *J. Phys. Chem.* **1989**, *93*, 4890−4894.
(36) Heck, K. N.; Janesko, B. G.; Scuseria, G. E.; Halas, N. J.; Wong, M. S. Observing Metal-Catalyzed Chemical Reactions in Situ Using Surface-Enhanced Raman Spectroscopy on Pd−Au Nanoshells. *J. Am. Chem. Soc.* **2008**, *130*, 16592−16600.
(37) Heck, K. N.; Janesko, B. G.; Scuseria, G. E.; Halas, N. J.; Wong, M. S. Using Catalytic and Surface-Enhanced Raman Spectroscopy-Active Gold Nanoshells to Understand the Role of Basicity in Glycerol Oxidation. *ACS Catal.* **2013**, *3*, 2430−2435.
(38) Xie, J.; Duan, P.; Kaylor, N.; Yin, K.; Huang, B.; Schmidt-Rohr, K.; Davis, R. J. Deactivation of Supported Pt Catalysts during Alcohol Oxidation Elucidated by Spectroscopic and Kinetic Analyses. *ACS Catal.* **2017**, *7*, 6745−6756.
(39) Duff, D. G.; Baiker, A.; Edwards, P. P. A New Hydrosol of Gold Clusters. 1. Formation and Particle Size Variation. *Langmuir* **1993**, *9*, 2301−2309.
(40) Aspnes, D. E. Analysis of Cermet Films with Large Metal Packing Fractions. *Phys. Rev. B: Condens. Matter Mater. Phys.* **1986**, *33*, 677−682.
(41) Degani, Y.; Sheng, T. T.; Heller, A.; Aspnes, D. E.; Studna, A. A.; Porter, J. D. "Transparent" Metals: Preparation and Characterization of Light-Transmitting Palladium, Rhodium, and Rhenium Films. *J. Electroanal. Chem. Interfacial Electrochem.* **1987**, *228*, 167−178.
(42) Kresse, G.; Furthmüller, J. Efficiency of Ab-Initio Total Energy Calculations for Metals and Semiconductors Using a Plane-Wave Basis Set. *Comput. Mater. Sci.* **1996**, *6*, 15−50.
(43) Perdew, J. P.; Burke, K.; Ernzerhof, M. Generalized Gradient Approximation Made Simple. *Phys. Rev. Lett.* **1996**, *77*, 3865−3868.
(44) Blöchl, P. E. Projector Augmented-Wave Method. *Phys. Rev. B: Condens. Matter Mater. Phys.* **1994**, *50*, 17953−17979.
(45) Kresse, G.; Joubert, D. From Ultrasoft Pseudopotentials to the Projector Augmented-Wave Method. *Phys. Rev. B: Condens. Matter Mater. Phys.* **1999**, *59*, 1758−1775.
(46) Methfessel, M.; Paxton, A. T. High-Precision Sampling for Brillouin-Zone Integration in Metals. *Phys. Rev. B: Condens. Matter Mater. Phys.* **1989**, *40*, 3616−3621.
(47) Monkhorst, H. J.; Pack, J. D. Special Points for Brillouin-Zone Integrations. *Phys. Rev. B: Solid State* **1976**, *13*, 5188−5192.
(48) Grimme, S. Semiempirical GGA-type density functional constructed with a long-range dispersion correction. *J. Comput. Chem.* **2006**, *27*, 1787−1799.
(49) Henkelman, G.; Uberuaga, B. P.; Jónsson, H. A Climbing Image Nudged Elastic Band Method for Finding Saddle Points and Minimum Energy Paths. *J. Chem. Phys.* **2000**, *113*, 9901−9904.
(50) Henkelman, G.; Jónsson, H. Improved Tangent Estimate in the Nudged Elastic Band Method for Finding Minimum Energy Paths and Saddle Points. *J. Chem. Phys.* **2000**, *113*, 9978−9985.
(51) Rumble, J. *CRC Handbook of Chemistry and Physics*; CRC Press, 2017.
(52) Jiang, Q.; Lu, H. M.; Zhao, M. Modelling of Surface Energies of Elemental Crystals. *J. Phys.: Condens. Matter* **2004**, *16*, 521−530.
(53) McQuarrie, D. A. *Statistical Mechanics*; University Science Books, 2000.
(54) Campbell, C. T.; Sellers, J. R. V. The Entropies of Adsorbed Molecules. *J. Am. Chem. Soc.* **2012**, *134*, 18109−18115.
(55) Perrin, D. D. *Ionisation Constants of Inorganic Acids and Bases in Aqueous Solution*; Pergamon Press: Oxford [Oxfordshire], New York, 1982.
(56) Mathew, K.; Sundararaman, R.; Letchworth-Weaver, K.; Arias, T. A.; Hennig, R. G. Implicit Solvation Model for Density-Functional Study of Nanocrystal Surfaces and Reaction Pathways. *J. Chem. Phys.* **2014**, *140*, 084106.
(57) Mathew, K.; Hennig, R. G. Implicit Self-Consistent Description of Electrolyte in Plane-Wave Density-Functional Theory. arXiv:1601.03346, **2016**.
(58) Campbell, C. T. The Degree of Rate Control: A Powerful Tool for Catalysis Research. *ACS Catal.* **2017**, *7*, 2770−2779.
(59) Campbell, C. T. Finding the Rate-Determining Step in a Mechanism. *J. Catal.* **2001**, *204*, 520−524.
(60) Shin, H.; Jung, S.; Bae, S.; Lee, W.; Kim, H. Nitrite Reduction Mechanism on a Pd Surface. *Environ. Sci. Technol.* **2014**, *48*, 12768−12774.
(61) Yin, Y. B.; Guo, S.; Heck, K. N.; Clark, C. A.; Coonrod, C. L.; Wong, M. S. Treating Water by Degrading Oxyanions Using Metallic Nanostructures. *ACS Sustainable Chem. Eng.* **2018**, *6*, 11160−11175.
(62) Huai, L.-y.; Su, T.; Wen, H.; Jin, X.; Liu, J.-y. NO Reduction by H2 on the Rh(111) and Rh(221) Surfaces: A Mechanistic and Kinetic Study. *J. Phys. Chem. C* **2016**, *120*, 5410−5419.
(63) Burch, R.; Daniells, S. T.; Hu, P. The Mechanism of N2O Formation via the (NO)2 Dimer: A Density Functional Theory Study. *J. Chem. Phys.* **2004**, *121*, 2737−2745.
(64) Qian, H.; Zhao, Z.; Velazquez, J. C.; Pretzer, L. A.; Heck, K. N.; Wong, M. S. Supporting Palladium Metal on Gold Nanoparticles Improves Its Catalysis for Nitrite Reduction. *Nanoscale* **2014**, *6*, 358−364.
(65) Barrabes, N.; Just, J.; Dafinov, A.; Medina, F.; Fierro, J.; Sueiras, J.; Salagre, P.; Cesteros, Y. Catalytic Reduction of Nitrate on Pt-Cu and Pd-Cu on Active Carbon Using Continuous Reactor: The Effect of Copper Nanoparticles. *Appl. Catal., B* **2006**, *62*, 77−85.
(66) Soares, O. S. G. P.; Orfão, J. J. M.; Pereira, M. F. R. Nitrate Reduction with Hydrogen in the Presence of Physical Mixtures with Mono and Bimetallic Catalysts and Ions in Solution. *Appl. Catal., B* **2011**, *102*, 424−432.
(67) Epron, F.; Gauthard, F.; Pinéda, C.; Barbier, J. Catalytic Reduction of Nitrate and Nitrite on Pt-Cu/Al2O3Catalysts in Aqueous Solution: Role of the Interaction between Copper and Platinum in the Reaction. *J. Catal.* **2001**, *198*, 309−318.
(68) Chen, Y.-X.; Zhang, Y.; Chen, G.-H. Appropriate Conditions or Maximizing Catalytic Reduction Efficiency of Nitrate into Nitrogen Gas in Groundwater. *Water Res.* **2003**, *37*, 2489−2495.
(69) Ebbesen, S.; Mojet, B.; Lefferts, L. In Situ ATR-IR Study of Nitrite Hydrogenation over Pd/Al2O3. *J. Catal.* **2008**, *256*, 15−23.
(70) Calvo, L.; Gilarranz, M. A.; Casas, A.; Mohedano, A. F.; Rodriguez, J. J. Denitrification of Water with Activated Carbon-Supported Metallic Catalysts. *Ind. Eng. Chem. Res.* **2010**, *46*, 5603−5609.
(71) Matsui, T.; Suzuki, S.; Katayama, Y.; Yamauchi, K.; Okanishi, T.; Muroyama, H.; Eguchi, K. In Situ Attenuated Total Reflection Infrared Spectroscopy on Electrochemical Ammonia Oxidation over Pt Electrode in Alkaline Aqueous Solutions. *Langmuir* **2015**, *31*, 11717−11723.
(72) Darvell, L. I.; Heiskanen, K.; Jones, J. M.; Ross, A. B.; Simell, P.; Williams, A. An Investigation of Alumina-Supported Catalysts for the Selective Catalytic Oxidation of Ammonia in Biomass Gasification. *Catal. Today* **2003**, *81*, 681−692.
(73) Singh, K. S.; Zhang, X. B.; Xu, Q. Room-Temperature Hydrogen Generation from Hydrous Hydrazine for Chemical Hydrogen Storage. *J. Am. Chem. Soc.* **2009**, *131*, 9894−9895.
(74) de Vooys, A. C. A.; Mrozek, M. F.; Koper, M. T. M.; van Santen, R. A.; van Veen, J. A. R.; Weaver, M. J. The Nature of Chemisorbates Formed from Ammonia on Gold and Palladium

DOI: 10.1021/acscatal.9b03239
ACS Catal. 2020, 10, 494−509

Electrodes as Discerned from Surface-Enhanced Raman Spectroscopy. *Electrochem. Commun.* **2001**, *3*, 293−298.
(75) Zhao, Y.; Koteswara Rao, N.; Lefferts, L. Adsorbed Species on Pd Catalyst during Nitrite Hydrogenation Approaching Complete Conversion. *J. Catal.* **2016**, *337*, 102−110.
(76) Chen, J. G.; Crooks, R. M.; Seefeldt, L. C.; Bren, K. L.; Bullock, R. M.; Darensbourg, M. Y.; Holland, P. L.; Hoffman, B.; Janik, M. J.; Jones, A. K.; Kanatzidis, M. G.; King, P.; Lancaster, K. M.; Lymar, S. V.; Pfromm, P.; Schneider, W. F.; Schrock, R. R. Beyond Fossil Fuel−Driven Nitrogen Transformations. *Science* **2018**, *360*, No. eaar6611.
(77) Bai, Y.; Mavrikakis, M. Mechanistic Study of Nitric Oxide Reduction by Hydrogen on Pt(100) (I): A DFT Analysis of the Reaction Network. *J. Phys. Chem. B* **2018**, *122*, 432−443.
(78) Farberow, C. A.; Dumesic, J. A.; Mavrikakis, M. Density Functional Theory Calculations and Analysis of Reaction Pathways for Reduction of Nitric Oxide by Hydrogen on Pt(111). *ACS Catal.* **2014**, *4*, 3307−3319.
(79) Huai, L.-y.; He, C.-z.; Wang, H.; Wen, H.; Yi, W.-c.; Liu, J.-y. NO Dissociation and Reduction by H2 on Pd(111): A First-Principles Study. *J. Catal.* **2015**, *322*, 73−83.
(80) Brown, W. A.; King, D. A. NO Chemisorption and Reactions on Metal Surfaces: A New Perspective. *J. Phys. Chem. B* **2000**, *104*, 2578−2595.
(81) He, Y.; Yu, J.; Wu, H.; Jia, J. Defining the Optimal Morphology of Rhn Nanoparticles for Efficient Hydrazine Adsorption: A DFT-D3 Study. *J. Mater. Sci.* **2019**, *54*, 9533−9542.
(82) Chan, H. Y. H.; Zou, S.; Weaver, M. J. Mechanistic Differences between Electrochemical and Gas-Phase Thermal Oxidation of Platinum-Group Transition Metals As Discerned by Surface-Enhanced Raman Spectroscopy. *J. Phys. Chem. B* **1999**, *103*, 11141−11151.
(83) Mamede, A.-S.; Leclercq, G.; Payen, E.; Grimblot, J.; Granger, P. Surface Raman Spectroscopic Study of NO Transformation over Pd-Based Catalysts. *Phys. Chem. Chem. Phys.* **2003**, *5*, 4402.
(84) Le Bourdon, G.; Adar, F.; Moreau, M.; Morel, S.; Reffner, J.; Mamede, A.-S.; Dujardin, C.; Payen, E. In Situ Characterization by Raman and IR Vibrational Spectroscopies on a Single Instrument: DeNO x Reaction over a Pd/γ-Al 2 O 3 Catalyst. *Phys. Chem. Chem. Phys.* **2003**, *5*, 4441−4444.
(85) Williams, C. T.; Tolia, A. A.; Chan, H. Y. H.; Takoudis, C. G.; Weaver, M. J. Surface-Enhanced Raman Spectroscopy as Anin SituReal-Time Probe of Catalytic Mechanisms at High Gas Pressures. *J. Catal.* **1996**, *163*, 63−76.
(86) Rae, S. I.; Khan, I. Surface Enhanced Raman Spectroscopy (SERS) Sensors for Gas Analysis. *Analyst* **2010**, *135*, 1365−1369.
(87) Tolia, A. A.; Williams, C. T.; Takoudis, C. G.; Weaver, M. J. Surface-Enhanced Raman Spectroscopy as an in-Situ Real-Time Probe of Catalytic Mechanisms at High Gas Pressures: The CO-NO Reaction on Rhodium. *J. Phys. Chem.* **1995**, *99*, 4599−4608.
(88) Gómez, R.; Rodes, A.; Pérez, J. M.; Feliu, J. M. FTIRS and Electrochemical Characterization of the NO Adlayer Generated by Immersion of a Rh(111) Electrode in an Acidic Solution of Nitrite. *J. Electroanal. Chem.* **1995**, *393*, 123−129.
(89) Williams, C. T.; Tolia, A. A.; Weaver, M. J.; Takoudis, C. G. Surface-Enhanced Raman Spectroscopy as an in-Situ Real-Time Probe of No Reduction over Rhodium at High Gas Pressures. *Chem. Eng. Sci.* **1996**, *51*, 1673−1682.
(90) Mamede, A.-S.; Leclercq, G.; Payen, E.; Granger, P.; Grimblot, J. In Situ Raman Characterisation of Surface Modifications during NO Transformation over Automotive Pd-Based Exhaust Catalysts. *J. Mol. Struct.* **2003**, *651-653*, 353−364.
(91) De Vooys, A. C. A.; Koper, M. T. M.; Van Santen, R. A.; Van Veen, J. A. R. Mechanistic Study on the Electrocatalytic Reduction of Nitric Oxide on Transition-Metal Electrodes. *J. Catal.* **2001**, *202*, 387−394.
(92) Halas, N. J.; Lal, S.; Chang, W.-S.; Link, S.; Nordlander, P. Plasmons in Strongly Coupled Metallic Nanostructures. *Chem. Rev.* **2011**, *111*, 3913−3961.
(93) Tolia, A. A.; Williams, C. T.; Weaver, M. J.; Takoudis, C. G. Surface-Enhanced Raman Spectroscopy as an in Situ Real-Time Probe of Catalytic Mechanisms at High Gas Pressures: The NO-H2 Reaction on Rhodium. *Langmuir* **1995**, *11*, 3438−3445.
(94) Gu, X.; Camden, J. P. Surface-Enhanced Raman Spectroscopy-Based Approach for Ultrasensitive and Selective Detection of Hydrazine. *Anal. Chem.* **2015**, *87*, 6460−6464.

DOI: 10.1021/acscatal.9b03239
ACS Catal. 2020, 10, 494−509